



Available online at www.sciencedirect.com



Icarus ●●● (●●●●) ●●●-●●●

ICARUS

www.elsevier.com/locate/icarus

## Updated Galileo probe mass spectrometer measurements of carbon, oxygen, nitrogen, and sulfur on Jupiter

Michael H. Wong,<sup>a,\*</sup> Paul R. Mahaffy,<sup>b</sup> Sushil K. Atreya,<sup>c</sup> Hasso B. Niemann,<sup>b</sup>  
and Tobias C. Owen<sup>d</sup>

<sup>a</sup> Astronomy Department, University of California at Berkeley, Berkeley, CA 94720-3411, USA

<sup>b</sup> Atmospheric Experiment Branch (Code 915), NASA Goddard Space Flight Center, Greenbelt, MD 20771, USA

<sup>c</sup> Department of Atmospheric, Oceanic, and Space Sciences, University of Michigan, Ann Arbor, MI 48109-2143, USA

<sup>d</sup> Institute for Astronomy, University of Hawaii, Honolulu, HI 96822, USA

Received 22 September 2003; revised 2 April 2004

### Abstract

The in situ measurements of the Galileo Probe Mass Spectrometer (GPMS) were expected to constrain the abundances of the cloud-forming condensable volatile gases: H<sub>2</sub>O, H<sub>2</sub>S, and NH<sub>3</sub>. However, since the probe entry site (PES) was an unusually dry meteorological system—a 5- $\mu$ m hotspot—the measured condensable volatile abundances did not follow the canonical condensation-limited vertical profiles of equilibrium cloud condensation models (ECCMs) such as Weidenschilling and Lewis (1973, *Icarus* 20, 465–476). Instead, the mixing ratios of H<sub>2</sub>S and NH<sub>3</sub> increased with depth, finally reaching well-mixed equilibration levels at pressures far greater than the lifting condensation levels, whereas the mixing ratio of H<sub>2</sub>O in the deep well-mixed atmosphere could not be measured. The deep NH<sub>3</sub> mixing ratio (with respect to H<sub>2</sub>) of  $(6.64 \pm 2.54) \times 10^{-4}$  from 8.9–11.7 bar GPMS data is consistent with the NH<sub>3</sub> profile from probe-to-orbiter signal attenuation (Folkner et al., 1998, *J. Geophys. Res.* 103, 22847–22856), which had an equilibration level of about 8 bar. The GPMS deep atmosphere H<sub>2</sub>S mixing ratio of  $(8.9 \pm 2.1) \times 10^{-5}$  is the only measurement of Jupiter's sulfur abundance, with a PES equilibration level somewhere between 12 and 15.5 bar. The deepest water mixing ratio measurement is  $(4.9 \pm 1.6) \times 10^{-4}$  (corresponding to only about 30% of the solar abundance) at 17.6–20.9 bar, a value that is probably much smaller than Jupiter's bulk water abundance. The <sup>15</sup>N/<sup>14</sup>N ratio in jovian NH<sub>3</sub> was measured at  $(2.3 \pm 0.3) \times 10^{-3}$  and may provide the best estimate of the protosolar nitrogen isotopic ratio. The GPMS methane mixing ratio is  $(2.37 \pm 0.57) \times 10^{-3}$ ; although methane does not condense on Jupiter, we include its updated analysis in this report because like the condensable volatiles, it was presumably brought to Jupiter in icy planetesimals. Our detailed discussion of calibration and error analysis supplements previously reported GPMS measurements of condensable volatile mixing ratios (Niemann et al., 1998, *J. Geophys. Res.* 103, 22831–22846; Atreya et al., 1999, *Planet. Space Sci.* 47, 1243–1262; Atreya et al., 2003, *Planet. Space Sci.* 51, 105–112) and the nitrogen isotopic ratio (Owen et al., 2001b, *Astrophys. J. Lett.* 553, L77–L79). The approximately three times solar abundance of NH<sub>3</sub> (along with CH<sub>4</sub> and H<sub>2</sub>S) is consistent with enrichment of Jupiter's atmosphere by icy planetesimals formed at temperatures < 40 K (Owen et al., 1999, *Nature* 402 (6759), 269–270), but would imply that H<sub>2</sub>O should be at least 3  $\times$  solar as well. An alternate model, using clathrate hydrates to deliver the nitrogen component to Jupiter, predicts O/H  $\geq 9 \times$  solar (Gautier et al., 2001, *Astrophys. J.* 550 (2), L227–L230). Finally we show that the measured condensable volatile vertical profiles in the PES are consistent with column-stretching or entraining downdraft scenarios *only* if the basic state (the pre-stretched column or the entrainment source region) is described by condensable volatile vertical profiles that are drier than those in the equilibrium cloud condensation models. This dryness is supported by numerous remote sensing results but seems to disagree with observations of widespread clouds on Jupiter at pressure levels predicted by equilibrium cloud condensation models for ammonia and H<sub>2</sub>S.

© 2004 Elsevier Inc. All rights reserved.

**Keywords:** Jupiter, atmosphere; Atmospheres, composition; Galileo probe

### 1. Introduction

The Galileo probe's in situ measurements provided a unique opportunity to sample Jupiter's atmosphere below

\* Corresponding author. Fax: +510-642-3411.  
E-mail address: mikewong@astro.berkeley.edu (M.H. Wong).

the cloud tops. In this paper we focus on the contribution of Galileo Probe Mass Spectrometer (GPMS) data to our understanding of the distribution of several of Jupiter's principal minor species: methane and the condensible volatiles ammonia, water, and hydrogen sulfide. The bulk abundances of these gases are crucial constraints on the formation of Jupiter. Our methane mixing ratio agrees with previous spectroscopic measurements, and our 9–12 bar  $\text{NH}_3$  mixing ratio confirms the approximately three times solar ammonia retrieved at that level from studies of the probe radio signal attenuation. No bulk abundance of  $\text{H}_2\text{S}$  has ever been obtained from remote sensing, so the GPMS measurement provides the only determination of Jupiter's sulfur abundance to date. The probe entry site (PES) was within a 5- $\mu\text{m}$  hotspot, an atypical region of Jupiter's atmosphere whose characteristics include reduced cloud opacity and condensible volatile mixing ratios. The variation in GPMS-derived  $\text{H}_2\text{S}$  and  $\text{H}_2\text{O}$  mixing ratios at depths far below the expected cloud levels for these gases yields one of the primary clues in the mystery of 5- $\mu\text{m}$  hotspot dynamics. Finally, we describe the analysis of GPMS data that provided the jovian  $\text{N}^{15}/\text{N}^{14}$  isotopic ratio presented in Owen et al. (2001b), a value that is consistent with measurements by ISO (Fouchet et al., 2000) and Cassini CIRS (Abbas et al., 2004; Fouchet et al., 2004).

In Section 2 we present our method of analysis of GPMS mixing ratios, with a full discussion of the sources of uncertainty in the data. The presentation of gas mixing ratios in Section 2 represents an incremental improvement over previously-reported GPMS results, with the primary contributions coming from the more thorough error analysis described in Sections 2.1–2.2, and a comprehensive correction for gas background contributions for water and ammonia. Niemann et al. (1998) (hereafter N98) gave the initial analysis of the GPMS data, and a detailed comparison between the present results and the N98 mixing ratios is given in Section 2.3.

Section 2.4 describes our determination of the  $^{15}\text{N}/^{14}\text{N}$  isotopic ratio. We use GPMS measurements of  $^{14}\text{NH}_3^{++}$  and  $^{15}\text{NH}_3^{++}$  at mass/charge values of 8.5 and 9 m/z, respectively (where m is in units of Dalton and  $z = 1$  for a singly charged ion), since the primary peak of  $^{15}\text{NH}_3$  at mass 18 is masked by the signal from  $\text{H}_2\text{O}$ . The GPMS determination of  $^{15}\text{N}/^{14}\text{N}$  is in excellent agreement with the most recent remote sensing results from the Cassini Composite Infrared Spectrometer (Fouchet et al., 2004; Abbas et al., 2004) but samples deeper in the atmosphere. Our concluding remarks in Section 3 support the conclusion of Owen et al. (2001b) that the jovian atmosphere has preserved the protosolar nitrogen isotopic ratio, a somewhat lower value than the ratios on terrestrial planets. The GPMS confirmed and/or discovered an approximately 3 times solar enrichment of nitrogen, sulfur, carbon, xenon, krypton, and argon, providing a key constraint on theories of the formation of Jupiter and the giant planets. In particular, the nitrogen and argon enrichments present a puzzle, because the enrichment requires the gases

to be present in the planetesimals that formed Jupiter in solar abundance, but neither nitrogen as  $\text{N}_2$  (probably the dominant carrier) nor argon are efficiently trapped in ice at the relatively warm (140 K) temperature at 5 AU in the protosolar nebula. Finally, we compare measured PES condensible volatile vertical profiles with column-stretching or entraining downdraft model results, and based on this comparison we conclude that condensible volatile profiles cannot be solely controlled by condensation as in the Weidenschilling and Lewis (1973) equilibrium cloud model, a conclusion that applies to the surroundings of the PES as well as to the PES itself. Additional mechanisms for modifying condensible volatile mixing ratios must be invoked, perhaps including molecular weight stratification as suggested by Guillot (1995).

## 2. Analysis

Previous GPMS publications have described the instrumentation (Niemann et al., 1992; 1996), earlier data analysis (Niemann et al., 1996, 1998; Mahaffy et al., 1999),  $^{15}\text{N}/^{14}\text{N}$  isotopic ratio (Owen et al., 2001b), and uncertainty estimates (Wong, 2001). We present an overview of GPMS data analysis considerations in Sections 2.1 and 2.2 that are relevant to the results presented in Section 2.3, noting advances provided in this paper. Although GPMS data analysis is not computationally or mathematically complex, meticulous care must be taken to properly account for distinct instrumental and physical effects. Most of the discussion here centers on the portions of the GPMS experiment that directly sampled Jupiter's atmosphere: the direct leak 1 (DL1) and direct leak 2 (DL2a and DL2b) sequences. Figure 1 shows the timing of mass spectrometer experiments during the probe descent, along with ambient temperature and pressure measurements from Seiff et al. (1998).

### 2.1. GPMS error analysis

The GPMS measured counts per integration period (counts  $\text{IP}^{-1}$ ) of all molecules, molecular fragments, and atoms at atomic mass-to-charge ratios from 2 to 150 m/z. For a mass-to-charge ratio of  $x$  m/z, we denote the measured counts per integration period as  $[x]$ . In order to distinguish between the effect of changes in abundance and the effect of changes in pressure on a particular count rate, we also require the counts per integration period,  $[\text{ref}]$ , of an atmospheric reference gas (N98). Then the number mixing ratio with respect to hydrogen,  $w_{\text{sp}}$ , of the atmospheric species can be derived using the relation

$$w_{\text{sp}} = \frac{n_{\text{sp}}}{n_{\text{H}_2}} = \text{cc}_{x/\text{ref}}^{\text{sp}} \frac{[x]}{[\text{ref}]} \equiv \text{cc}_{x/\text{ref}}^{\text{sp}} [x/\text{ref}], \quad (1)$$

where cc is called the calibration constant for historical reasons (even though it actually varies with pressure for some gases), and  $[x/\text{ref}]$  denotes the count ratio  $[x]/[\text{ref}]$ . Calibration constants are obtained from experiments performed

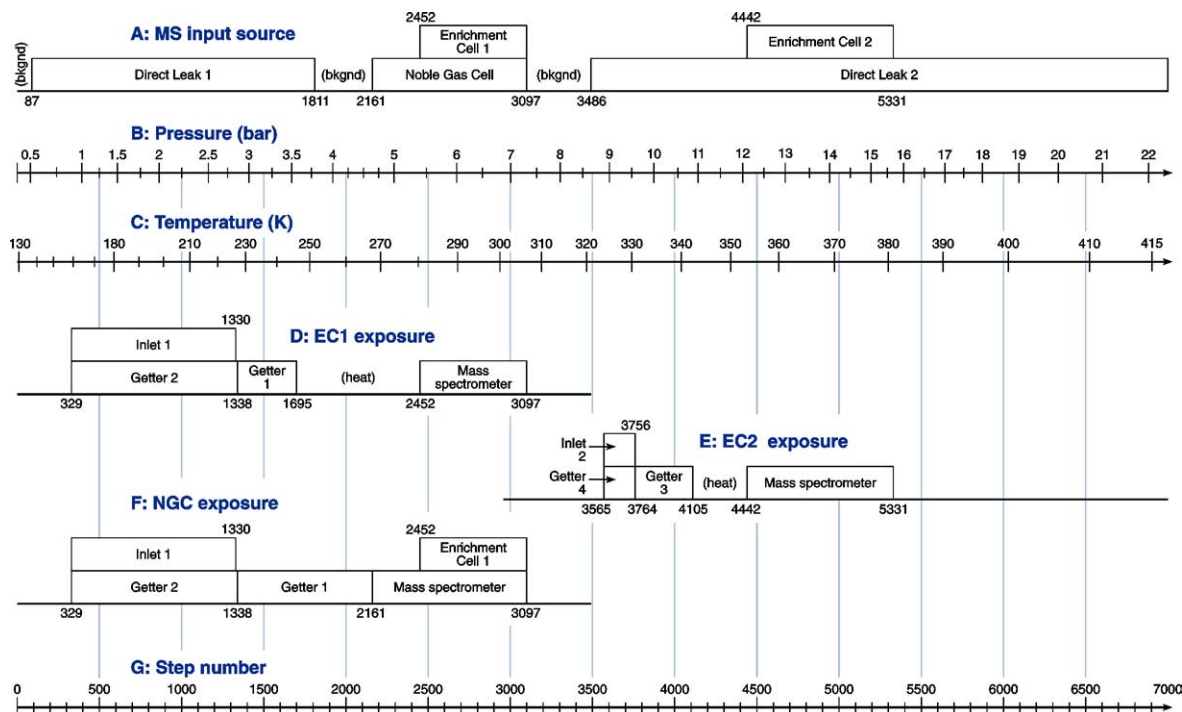


Fig. 1. GPMS experimental sequence. The source sampled by the mass spectrometer is shown in (A), as a function of sequence step number (G; each step is 0.5 sec). Enrichment experiment events are shown in (D), (E), and (F), where removal of much of the hydrogen from the sampled gas allowed the detection limit for various heavier gases to be substantially decreased (see Niemann et al., 1992, 1998, for more information). Descent pressure (B) and temperature (C) profiles are taken from Seiff et al. (1998).

using either the GPMS flight unit (FU) in 1985 before the launch of Galileo, or the experimental unit (EU), an identical spare instrument that is currently still functioning at NASA GSFC. Calibration constants for methane, ammonia,  $\text{H}_2\text{S}$ , and water are discussed below. Fits to the calibration data showed a dependence on pressure for  $\text{cc}_{34/\text{ref}}^{\text{H}_2\text{S}}$  and  $\text{cc}_{18/\text{ref}}^{\text{H}_2\text{O}}$ . For ammonia,  $\text{cc}_{17/\text{ref}}^{\text{NH}_3}$  was found to be constant with pressure, although some variation was seen as a function of the ammonia mole fraction in the calibration gas mixture. Calibration constants are derived from calibration experiment count ratios and mixing ratios via the formula:

$$\text{cc}_{x/\text{ref}}^{\text{sp}} \equiv \left. \frac{[\text{ref}]}{[x]} \right|_{\text{lab}} \left. \frac{n_{\text{sp}}}{r_{\text{ref}}} \right|_{\text{lab}} \left. \frac{n_{\text{ref}}}{n_{\text{H}_2}} \right|_{\text{Jup}} \quad (2)$$

Estimation of GPMS mixing ratio uncertainties involves combining several distinct error contributions from every factor in Eqs. (1) and (2). We discuss each source of uncertainty individually below.

A separate background count rate was subtracted for each value of the mass to charge ratio in the GPMS data. In order to measure this background contribution, measurements were taken at specific intervals during the probe descent, with the mass spectrometer isolated from all gas sources (denoted as “bkgnd” in Fig. 1; see also Wong, 2001). For [34], the main peak of  $\text{H}_2\text{S}$ , a constant background level was subtracted, but for water, ammonia, and methane, exponentially decaying contributions were subtracted. The uncertainty in this background level contributes to the error both in GPMS descent count ratios as well as in calibration exper-

iment count ratios, but is significant mainly for gases with large exponentially decaying background contributions such as ammonia and water, and gases with very low count rates of on the order of  $100 \text{ counts IP}^{-1}$  or less.

Poisson-distributed statistical noise, with a theoretical measurement uncertainty equal to the square root of the counting rate, is significant mainly for data in the range of  $100 \text{ counts IP}^{-1}$  or less. In the GPMS, the statistical uncertainty departs from the Poisson distribution and reaches an approximately constant value of 0.49% at high counting rates, but at these high count rates, statistical noise is by far the smallest source of uncertainty.

At high count rates (see below), the uncertainty in the deadtime correction constant,  $\tau$ , becomes an important source of error. An equation commonly used to provide a deadtime correction for pulse counting systems,

$$[x]_{\text{obs}} = [x]_{\text{in}} e^{-\tau[x]_{\text{in}}}, \quad (3)$$

was found to well represent the behavior of the GPMS ion counting detector system, where  $[x]_{\text{in}}$  are ions incident on the detector and  $[x]_{\text{obs}}$  are the observed counts. This deadtime effect is a result of the finite recovery time of the pulse counting system; during the recovery “deadtime” any incoming ions are not counted (see Fig. 2). At high detector ion currents, an appreciable fraction of the counts will be lost during the detector deadtime. As the incident ions continually increase, observed counts will reach a maximum (at the detector saturation point) and then begin to decrease. Equation (3) can be differentiated and solved for  $\tau$  in terms of the

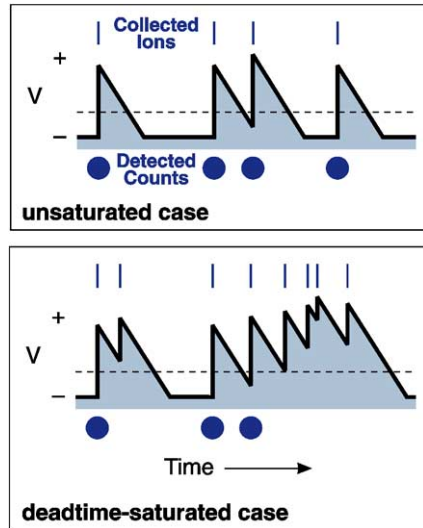


Fig. 2. Illustration of pulse pile-up that contributes to the loss of detector efficiency at high count rates. The current pulse produced for each ion reaching the detector is converted to a voltage pulse by the pulse amplifier circuit and measured by a threshold detector. For those cases where the signal does not drop below this threshold (horizontal dashed line) at high ion currents, the ion pulse is not counted. Equation (3) corrects for this effect.

observed counts at detector saturation  $\max([x]_{\text{obs}})$ :

$$\tau = \frac{1}{e \cdot \max([x]_{\text{obs}})}. \quad (4)$$

Thus any mass spectrometer dataset that exhibits detector saturation can yield an estimate of the deadtime constant, which has units of IP counts<sup>-1</sup>. The GPMS had a 0.5-sec integration period.

The detector deadtime characteristics are different for every detector, so it is essential to determine the appropriate deadtime correction for a given detector using data taken from that same detector. In addition, some laboratory experiments demonstrated a change in the deadtime correction over time. For the flight unit, two datasets are used to determine the appropriate correction. In the proto-flight experiment (PFU) conducted in the laboratory before launch, [2] approached a maximum of 10,788,864 counts IP<sup>-1</sup>. Near 11 bar in the probe descent, interpolation of [2] data indicate a maximum of 8,520,851 counts IP<sup>-1</sup>. For correcting flight-unit data, we use the mean of the deadtime constants calculated from these count maxima and use the difference as an estimate of the 2- $\sigma$  uncertainty in the result, i.e.,  $\tau = 3.86 \times 10^{-8}$  with a 1- $\sigma$  uncertainty of 12%.

Since implementing the deadtime correction involves numerically solving Eq. (3), we have no analytical expression for the uncertainty in a count ratio resulting from uncertainty in the deadtime coefficient. Rather, in order to estimate the relative error  $\sigma_{\text{CR}}$  in the deadtime-corrected count ratio  $[x/\text{ref}]'$  due to a change  $\Delta\tau$  in the deadtime coefficient  $\tau$ , we take the following approach:

$$\sigma_{\text{CR}} \equiv \frac{[x/\text{ref}]'_{\tau} - [x/\text{ref}]'_{\tau+\Delta\tau}}{[x/\text{ref}]'_{\tau}}, \quad (5)$$

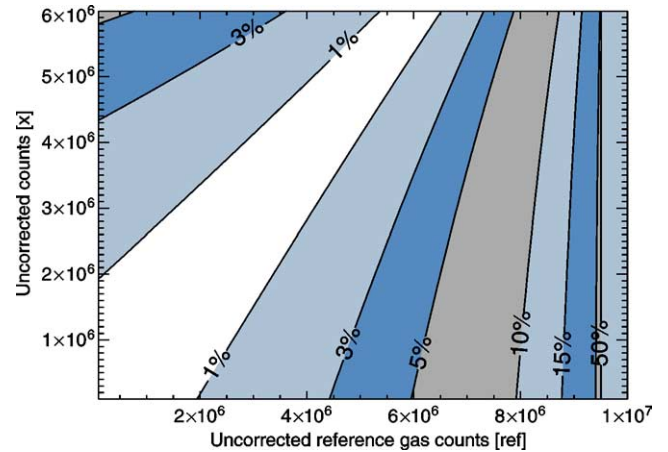
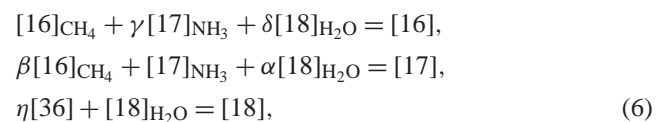


Fig. 3. Contours show the uncertainty in GPMS count ratio  $[x/\text{ref}]$  as a bivariate function of  $[x]$  and  $[\text{ref}]$ , due to the uncertainty in the deadtime coefficient, assuming a deadtime coefficient of  $\tau_m = (3.86 \pm 0.46) \times 10^{-8}$ .

where the deadtime coefficient used to correct each count ratio is indicated as either  $\tau$  or  $\tau + \Delta\tau$ . Figure 3 shows a plot of the quantity  $\sigma_{\text{CR}}$  as a bivariate function of uncorrected count rates  $[x]$  and  $[\text{ref}]$ , for an uncertainty of  $\sigma_{\tau} = 12\%$  and  $\tau = 3.86 \times 10^{-8}$ . Note that as  $[\text{ref}]$  increases towards the asymptote located at  $9.5 \times 10^6$ , the uncertainty increases rapidly. This asymptote is the maximum in observed counts corresponding to the deadtime constant chosen; using different values of  $\tau$  will move the location of the asymptote. Using different values of  $\sigma_{\tau}$  will change the scale on the contours. Regardless of the values of  $\tau$  and  $\sigma_{\tau}$ , the lowest errors caused by deadtime uncertainty occur either when the count ratio is close to unity (the diagonal white stripe in Fig. 3), or when uncorrected count rates are low (i.e.,  $[x] \leq 5 \times 10^6$  counts IP<sup>-1</sup>).

Neutral molecules entering the mass spectrometer are ionized by an electron beam, with most molecules splitting into fragments and producing peaks at several different mass to charge ratios. Mass interference can be a problem when multiple gases have peaks at the same mass. Figure 4 shows the overlapping mass spectra of ammonia, water, methane, and argon, with the primary peak of each gas normalized to unity. Data for these spectra were obtained in EU experiments, and both the experiments and the GPMS Jupiter data presented here used an ionization energy of 75 eV. The fragmentation patterns in Fig. 4 are molecular properties that theoretically should be a function only of the energy of the ionizing electron beam. A mass spectrum of a gas sample containing water, ammonia, methane, and argon will be a linear combination of the fragmentation patterns in Fig. 4, and can be represented algebraically as:



where for example [17] represents observed counts at  $m/z = 17$ , and  $[17]\text{NH}_3$  are the corrected counts due only to ammo-

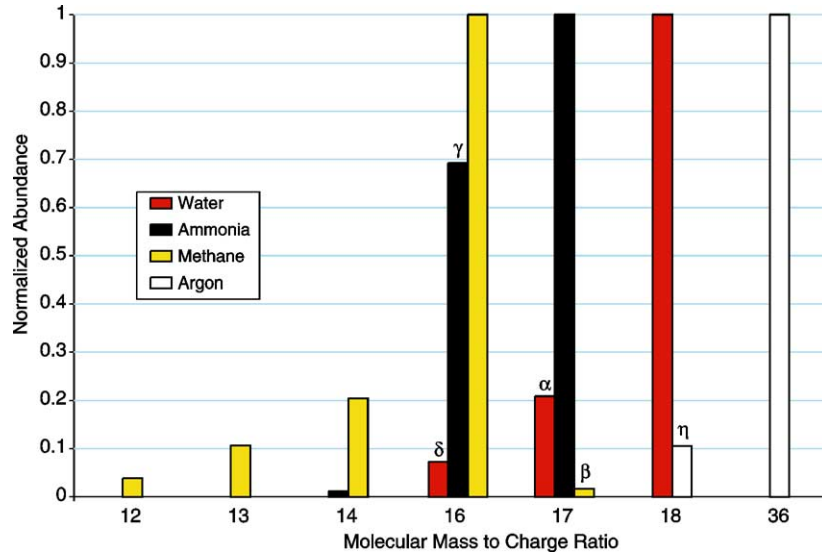


Fig. 4. Normalized mass spectrum of water, ammonia, methane, and argon, as a function of mass-to-charge ratio. Data sources are EU experiments (argon, water, ammonia) and the NIST MSDB v4.5 (methane). Fractions labeled by Greek letters correspond to constants used in Eqs. (6) and (7).

nia. Then solving for the corrected counts  $[17]_{\text{NH}_3}$  in terms of the splitting fractions and the observed counts yields:

$$[17]_{\text{NH}_3} = \frac{[17] - \beta[16] - (\alpha - \beta\delta)([18] - \eta[36])}{1 - \beta\gamma}. \quad (7)$$

In the EU experiment which was used to determine the methane fragmentation pattern, splitting fraction measurements had standard deviations ranging from 0.6 to 2.9%. Comparing fragmentation patterns obtained from both the GPMS EU and the MSDB v4.5 (NIST/EPA/NIH Mass Spectral Database, version 4.5, 1994, Gaithersburg MD: U.S. Department of Commerce) reveals differences for many gases on the order of 10%. In fact, for many molecules the MSDB contains fragmentation pattern records obtained by different laboratories, and 0–10% discrepancies in fragmentation pattern values are typical. However, since the GPMS experimental unit and flight units were very similar, we do not expect such a large difference between the fragmentation patterns they produce. Thus for fragmentation patterns used in this analysis, we assume an average relative uncertainty for all splitting fractions of 5% (e.g.,  $\sigma_\beta = 0.05\beta$ ). This assumed uncertainty is an intermediate case between the 0.6–2.9% standard deviation of methane splitting fractions in the EU, and the differences on the order of 10% from instrument to instrument as seen in the MSDB.

## 2.2. GPMS calibration constants

One of the primary sources of uncertainty in every GPMS mixing ratio is the calibration constant, defined in Eqs. (1) and (2). Laboratory calibration experiments discussed here were done between 1996 and 2000, using the flight spare experimental unit. Calibration constant data are shown in Figs. 5 through 8. Calibration constants for each gas under consideration will be discussed separately below. In each plot in Figs. 5 through 8, the y-axis is calibration constant,

and the x-axis is pressure in the laboratory gas circulation system. Lines connect calibration constant values that were taken in a single calibration experimental run. The fitted calibration constants, which we use in the final GPMS mixing ratio analyses, are depicted as thick black lines, with light shading indicating the  $1-\sigma$  uncertainty envelope in the fitted calibration constants. Vertical shaded stripes labeled “DL1,” “DL2a,” and “DL2b” represent the pressure ranges in the calibration runs corresponding to the intervals of probe data that directly sampled the jovian atmosphere (see Fig. 1). In Table 1, details of the individual calibration runs are presented. In experiments listed in Table 1 as following a descent simulation, pressure was increased over time. In earlier experiments (no descent simulation), laboratory gas pressures decreased with time.

Figure 5 shows calibration data for methane, which we measure using both the  $[16/4]$  (panels (A) and (B)) and  $[13/4]$  (panels (C) and (D)) count ratios. For direct leak 1 (panels (A) and (C)), methane calibration constants exhibit an initial decrease with pressure/time, followed by a more constant phase. To obtain the final DL1 calibration constants, we averaged only the last several points of each calibration run, to reduce the influence of the low-pressure transient effect. For the DL2 data however (panels (B) and (D)), observed calibration constants were largely constant, so all datapoints were included in the final average. We first obtained an average calibration constant for each individual calibration run, and then took the mean of these averages to get the final value. Then the standard deviations in the final averages reflect the variation in the calibration constants from experiment to experiment, providing the best estimate of the uncertainty in the calibration constants. We find  $cc_{16/4}^{\text{CH}_4} = (1.38 \pm 0.21) \times 10^{-2}$  in DL1 and  $(1.20 \pm 0.22) \times 10^{-2}$  in DL2, and  $cc_{13/4}^{\text{CH}_4} = 0.428 \pm 0.084$  in DL1 and  $0.469 \pm 0.099$  in DL2.

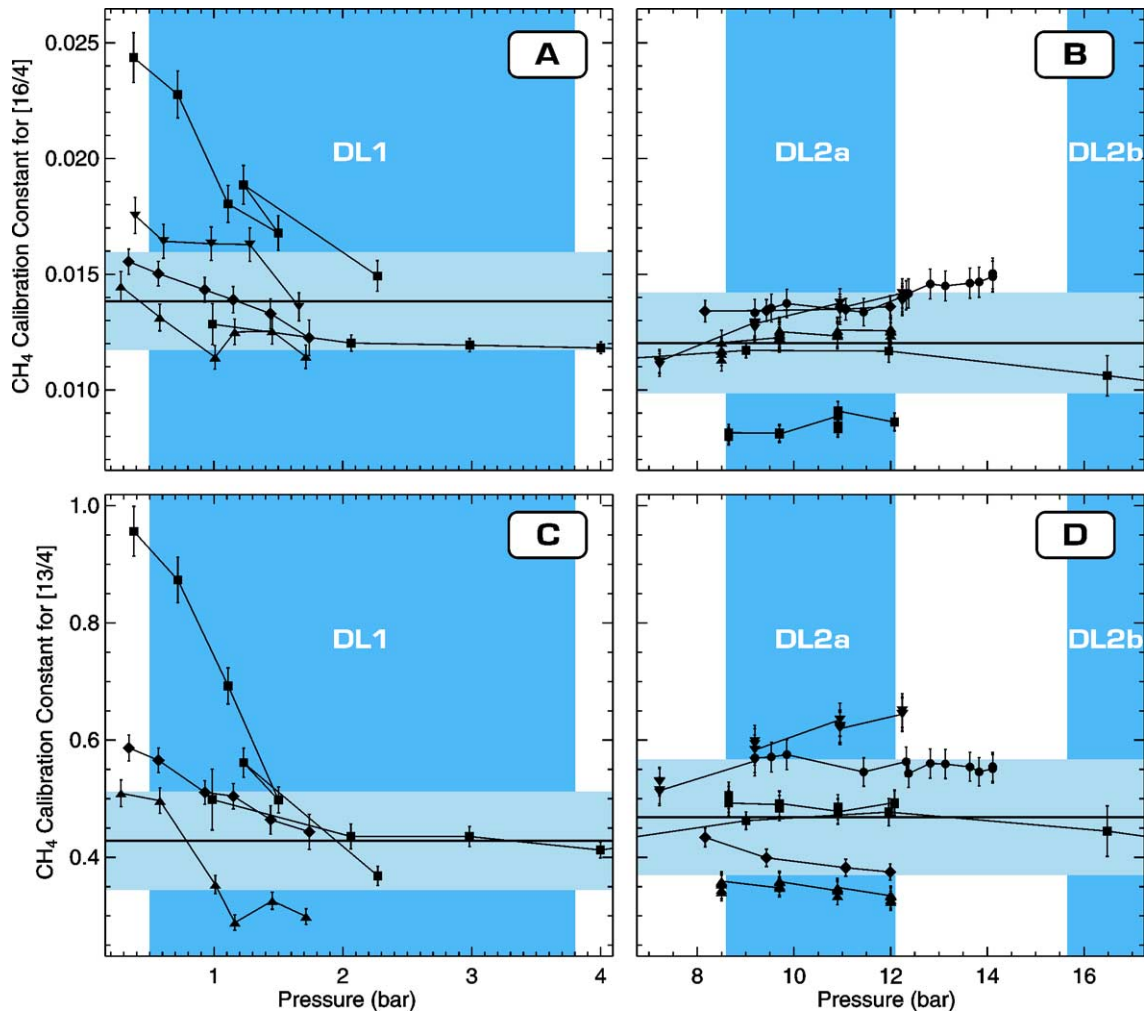


Fig. 5. GPMS calibration constants for methane as a function of pressure in the laboratory gas handling system. Panels (A) and (B) show calibration constants for the [16/4]; panels (C) and (D) are for [13/4] calibration. Panels (A) and (C) apply to direct leak 1 (DL1) measurements; panels (B) and (D) are for DL2 measurements. Dark shaded regions, labeled DL1, DL2a, and DL2b, show pressures corresponding to the GPMS descent data. Solid horizontal lines in each panel show average calibration constants, and the light shaded areas show the uncertainty in this average, presuming that the scatter is entirely due to an unknown systematic effect on the calibration experiments that affects each individual experiment coherently.

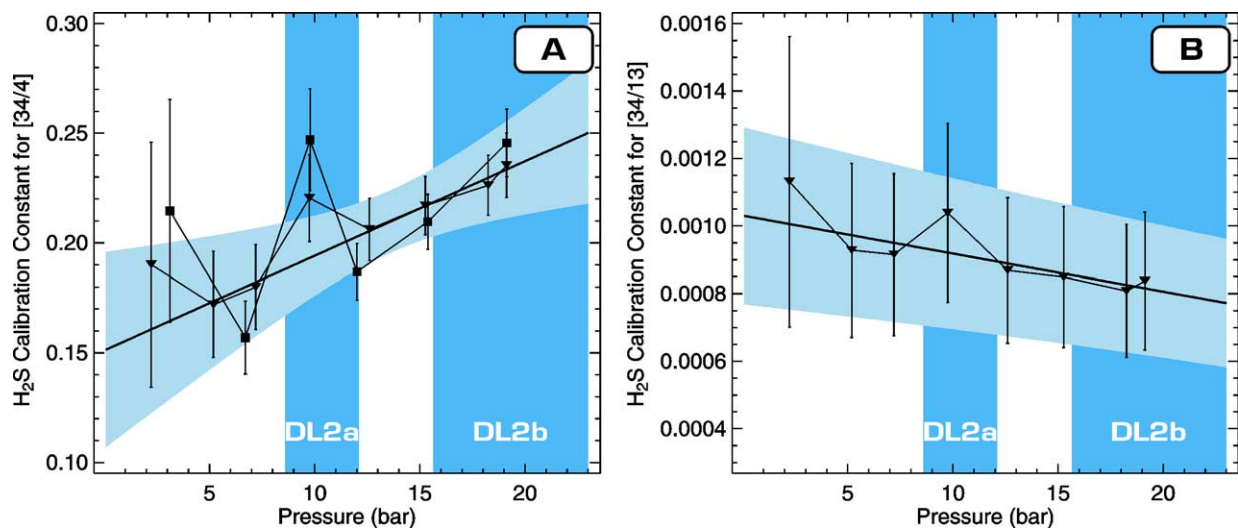


Fig. 6. GPMS calibration constants for hydrogen sulfide, for direct leak 2 data. Squares show data from experiment EU-961123 (Table 1), and triangles show data from experiment EU-961129. Panel (A) shows calibration constants for the [34/4] count ratio; panel (B) is for [34/13] calibration.

Table 1  
Calibration experiments

Experiment	Gas mole fraction						Calibration constants	Leaks	Descent simulation
	H <sub>2</sub>	He	CH <sub>4</sub>	NH <sub>3</sub>	H <sub>2</sub> O	H <sub>2</sub> S			
EU-001006	$8.63 \times 10^{-1}$	$1.31 \times 10^{-1}$	$2.16 \times 10^{-3}$	$4.81 \times 10^{-4}$		0	CH <sub>4</sub> , NH <sub>3</sub>	2	yes
EU-000808	$8.58 \times 10^{-1}$	$1.43 \times 10^{-1}$	$1.77 \times 10^{-3}$	$4.26 \times 10^{-4}$		0	CH <sub>4</sub> , NH <sub>3</sub>	1, 2	yes
EU-000630	$8.63 \times 10^{-1}$	$1.305 \times 10^{-1}$	$2.06 \times 10^{-3}$	$2.42 \times 10^{-4}$		0	CH <sub>4</sub> , NH <sub>3</sub>	1, 2	yes
EU-990513	$8.62 \times 10^{-1}$	$1.35 \times 10^{-1}$	$1.83 \times 10^{-3}$	$2.10 \times 10^{-4}$	$2.08 \times 10^{-5}$	0	CH <sub>4</sub> , NH <sub>3</sub>	1, 2	yes
EU-990428	$8.60 \times 10^{-1}$	$1.36 \times 10^{-1}$	$1.80 \times 10^{-3}$	$2.30 \times 10^{-4}$	$2.07 \times 10^{-5}$	0	CH <sub>4</sub>	1, 2	yes
EU-970630L1	$8.71 \times 10^{-1}$	$1.27 \times 10^{-1}$	$1.96 \times 10^{-3}$	0	0	0	CH <sub>4</sub>	1	no
EU-970630L2	$8.67 \times 10^{-1}$	$1.31 \times 10^{-1}$	$2.07 \times 10^{-3}$	0	0	0	CH <sub>4</sub>	2	no
MIX97_D	$8.88 \times 10^{-1}$	$1.10 \times 10^{-1}$	$1.90 \times 10^{-3}$	$9.00 \times 10^{-4}$	$6.95 \times 10^{-5}$	0	H <sub>2</sub> O	2	no
MIX97_G	$8.88 \times 10^{-1}$	$1.10 \times 10^{-1}$	$1.87 \times 10^{-3}$	$8.79 \times 10^{-4}$	$6.86 \times 10^{-5}$	0	H <sub>2</sub> O	2	no
MIX97_H	$8.87 \times 10^{-1}$	$1.10 \times 10^{-1}$	$1.92 \times 10^{-3}$	$9.57 \times 10^{-4}$	$1.33 \times 10^{-4}$	0	H <sub>2</sub> O	2	no
MIX97_K	$8.64 \times 10^{-1}$	$1.34 \times 10^{-1}$	$1.91 \times 10^{-3}$	$2.29 \times 10^{-4}$	$6.82 \times 10^{-5}$	0	H <sub>2</sub> O	2	no
MIX97_L	$8.64 \times 10^{-1}$	$1.34 \times 10^{-1}$	$1.91 \times 10^{-3}$	0	$6.93 \times 10^{-5}$	0	H <sub>2</sub> O	2	no
MIX97_N	$8.65 \times 10^{-1}$	$1.32 \times 10^{-1}$	$1.89 \times 10^{-3}$	$2.38 \times 10^{-3}$	$6.85 \times 10^{-5}$	0	H <sub>2</sub> O	2	no
MIX97_S	$8.64 \times 10^{-1}$	$1.34 \times 10^{-1}$	$1.89 \times 10^{-3}$	0	$1.33 \times 10^{-4}$	0	H <sub>2</sub> O	2	no
MIX97_U	$8.64 \times 10^{-1}$	$1.34 \times 10^{-1}$	$1.90 \times 10^{-3}$	$2.32 \times 10^{-4}$	$1.32 \times 10^{-4}$	0	H <sub>2</sub> O	2	no
MIX97_Y	$8.66 \times 10^{-1}$	$1.30 \times 10^{-1}$	$1.89 \times 10^{-3}$	$2.22 \times 10^{-3}$	$1.32 \times 10^{-4}$	0	H <sub>2</sub> O	2	no
EU-961129	$8.61 \times 10^{-1}$	$1.37 \times 10^{-1}$	$1.59 \times 10^{-3}$	0	0	$2.15 \times 10^{-5}$	H <sub>2</sub> S	2	no
EU-961123	$8.62 \times 10^{-1}$	$1.39 \times 10^{-1}$	0	0	0	$2.17 \times 10^{-5}$	H <sub>2</sub> S	1, 2	no

The H<sub>2</sub>S calibration constants  $cc_{34/4}^{H_2S}$  and  $cc_{34/13}^{H_2S}$  are shown in Fig. 6. For experiment EU-961129 (triangles in Fig. 6; see also Table 1), both methane and helium were included in the calibration gas mixture, so calibration constants were derived for both reference gases. Helium was the only reference gas present in the EU-961123 calibration mixture, so calibration constants were derived only for the count ratio [34/4]. The two runs are in good agreement for  $cc_{34/4}^{H_2S}$ . We tested the linear correlation coefficients (Bevington and Robinson, 1992, p. 199) for both the  $cc_{34/4}^{H_2S}$  and  $cc_{34/13}^{H_2S}$  datasets, finding in both cases an approximate 98% probability that the calibration constants are linearly correlated with pressure. For the  $cc_{34/13}^{H_2S}$  data shown in Fig. 6B, the largest contribution to the plotted uncertainties comes from the uncertainty in the jovian methane mixing ratio. Since this uncertainty has a coherent systematic effect on all the datapoints, it is an indication of the uncertainty in the value of the final calibration constant rather than an indication of an uncertainty in the functional form of the fit. The observed contrast in slope between the  $cc_{34/4}^{H_2S}$  and  $cc_{34/13}^{H_2S}$  calibration constants is due to the pressure dependence of the counts from the reference gases helium and methane. From Eq. (2), it follows that

$$\frac{cc_{34/4}^{H_2S}}{cc_{34/13}^{H_2S}} \sim \frac{[4]}{[13]} \sim cc_{13/4}^{CH_4}, \quad (8)$$

so the difference in the sign of the slopes of  $cc_{34/4}^{H_2S}$  and  $cc_{34/13}^{H_2S}$  is consistent with our finding that  $cc_{13/4}^{CH_4}$  is constant with pressure.

Figure 7 shows data from nine calibration experiments for water, for the [18/13] count ratio. As with the calibration constants for H<sub>2</sub>S, we find that  $cc_{18/13}^{H_2O}$  depends on pressure. Water mole fractions in these experiments ranged from

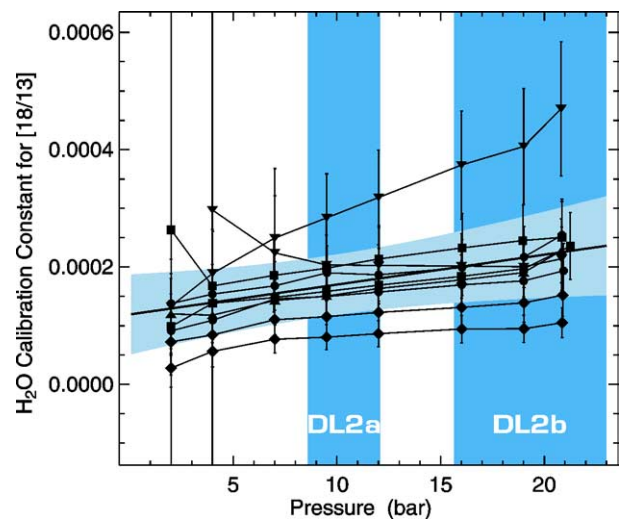


Fig. 7. Pressure-varying GPMS calibration constants for water. Nine calibration runs were combined to obtain the fits, with calibration mixtures containing water mole fractions of about  $7 \times 10^{-5}$  and  $1.3 \times 10^{-4}$ , as well as varying abundances of ammonia and near-jovian abundances of hydrogen, helium, and methane (see Table 1).

$6.8 \times 10^{-5}$  to  $1.3 \times 10^{-4}$  (see Table 1). We noticed a variation in the water calibration constant as a function of the water mole fraction in the experimental gas mixture, so the calibration runs shown here were chosen because they provide a closer match to the retrieved PES water mole fractions than the calibration runs with water mole fractions of  $4 \times 10^{-5}$  and  $10^{-3}$  (described in Wong, 2001, but not shown here).

Measuring ammonia mixing ratios with the mass spectrometer is very challenging due to the strong wall interactions between polar NH<sub>3</sub> molecules and the vacuum pumping system; ammonia essentially “sticks” to the walls. For this reason, only one of the three GPMS direct atmospheric

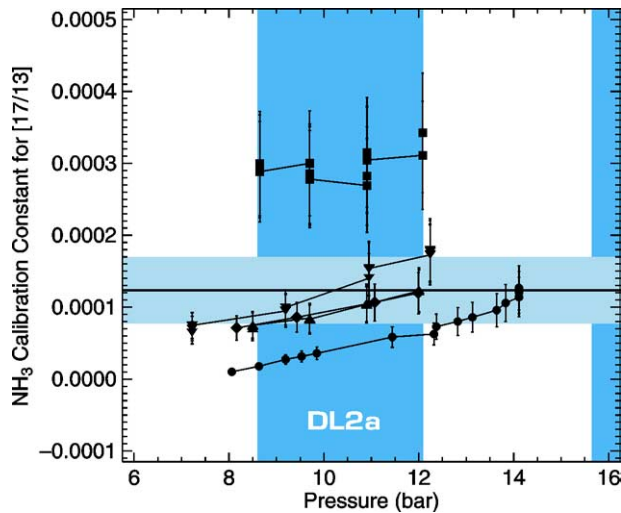


Fig. 8. GPMS calibration constants for ammonia. Exponentially decaying background corrections have already been subtracted from the data. Experiment EU-000630 (squares) was excluded from the final average but is shown here for completeness (see Section 2.2).

measurements yields a useful result. For the DL1 experiment, the indirect beaming of gas into the mass spectrometer prevented ammonia measurements (Niemann et al., 1996). Shortly before the DL2a and DL2b experiments, enrichment cell experiments saturated the system with large amounts of ammonia (Fig. 1). Then at the beginning of DL2a and DL2b, the influx of hydrogen from Jupiter's atmosphere acted to desorb the ammonia remaining in the GPMS and produced large ammonia background residuals that contaminated the direct atmospheric signal. These residuals decay with time, and for DL2a we are able to model the direct atmospheric and time-dependent background components, such that

$$[17] = [17]' + \alpha \exp(\beta t), \quad (9)$$

where the constant  $[17]$  is our estimate of the direct atmospheric component. Several other functional forms were tried, including terms in  $[17]$  that were proportional to time or to reference gas counts such as  $[13]$ . From all the functional forms tested, we selected Eq. (9) because it is simplest and because it gives the best fit (i.e., lowest value of  $\chi^2$ ) to the GPMS DL2a data. The descent simulation used in the ammonia calibration runs (Fig. 8) included an enrichment cell 1 and noble gas cell simulation, which flooded the EU mass spectrometer with ammonia, so that the background residuals for the DL2a calibration would be analogous to the DL2a flight data. Calibration data displayed in Fig. 8 have already been corrected for this background contribution. The parameters  $\alpha$  and  $\beta$  in Eq. (9) varied from run to run, but in each case the background residual was larger than  $[17]'$  for the first two to six minutes. Note that calibration constant values seem to increase with pressure in Fig. 8. The increase can be understood as an artifact of the functional form of our background residual; since we assume a constant  $[17]'$ , and reference gas counts  $[13]$  increase with pressure, the calibration constant must increase with pressure (by the definition

of  $cc$  in Eq. (2)). Given the magnitude of the background correction and the scatter from calibration run to calibration run, we chose to fit the ammonia calibration constant as an average value. Calibration constants for experiment EU-000630 (squares in Fig. 8) were considerably larger than for other experiments, so the data are shown but not included in our preferred average calibration constant value of  $cc_{17/13}^{\text{NH}_3} = (1.23 \pm 0.46) \times 10^{-4}$ . Inclusion of EU-000630 data would increase both the calibration constant value and uncertainty to  $cc_{17/13}^{\text{NH}_3} = (1.58 \pm 0.92) \times 10^{-4}$ , but the doubling of the uncertainty provides justification for dropping the EU-000630 data as an outlier.

### 2.3. GPMS mixing ratios

#### 2.3.1. Methane mixing ratio

The methane mixing ratio at Jupiter is displayed in Fig. 9. Triangles show mixing ratios derived from  $[16/4]$ , and circles show mixing ratios derived from  $[13/4]$ . Squares in Fig. 9 show the methane mixing ratio derived from  $[16/4]$  without performing the correction for mass interference from other gases. Since there was no ammonia or water signal in DL1 (0.5 to 3.8 bar), the mass interference correction is significant only in DL2a. The methane mixing ratio derived from  $[16/4]$  is the same in DL1 and DL2a, while the mixing ratio derived from  $[13/4]$  is 10% higher in DL1 and 20% higher in DL2a. Because higher  $[4]$  in DL2a leads to larger deadtime correction errors, and the disagreement between  $[13/4]$  and  $[16/4]$  is greater in DL2a, we obtain our preferred methane mixing ratio using the DL1 data. The lower mixing ratios at pressures less than about 1.25 bar are due to the same transient effect that in the laboratory leads to the larger calibration constant values seen at similar pressures in Fig. 5, so our mixing ratio averages exclude points at pressures less than 1.25 bar in DL1. The average methane mixing ratio is  $(2.55 \pm 0.62) \times 10^{-3}$  obtained from  $[13/4]$  alone and  $(2.33 \pm 0.55) \times 10^{-3}$  obtained from  $[16/4]$  alone. Our preferred value, listed in Table 2, is  $(2.37 \pm 0.57) \times 10^{-3}$  obtained from both  $[16/4]$  and  $[13/4]$  in DL1. This methane mixing ratio is comparable to mixing ratios from independent analyses, such as  $(1.95 \pm 0.22) \times 10^{-3}$  from the Voyager IRIS analysis of Gautier et al. (1982) and  $(2.5 \pm 0.4) \times 10^{-3}$  from ground-based spectra in the 1100–1200  $\text{cm}^{-1}$  range by Knacke et al. (1982). Previous analyses of GPMS data yielded  $(2.1 \pm 0.4) \times 10^{-3}$  in N98 and  $(1.982 \pm 0.048) \times 10^{-3}$  in Wong et al. (1999). The current result benefits from both improved calibration experiments (including the simulation of the pressure increase over time) as well as a more comprehensive error analysis, so although it is not normally considered progress to enlarge uncertainties in a result, we consider the current result a more fair estimation of the possible error than the previously published estimates. Using Anders and Grevesse (1989) as a reference for this and all other solar composition comparisons in this paper, our analysis yields a supersolar jovian methane enrichment of  $3.27 \pm 0.78$ .

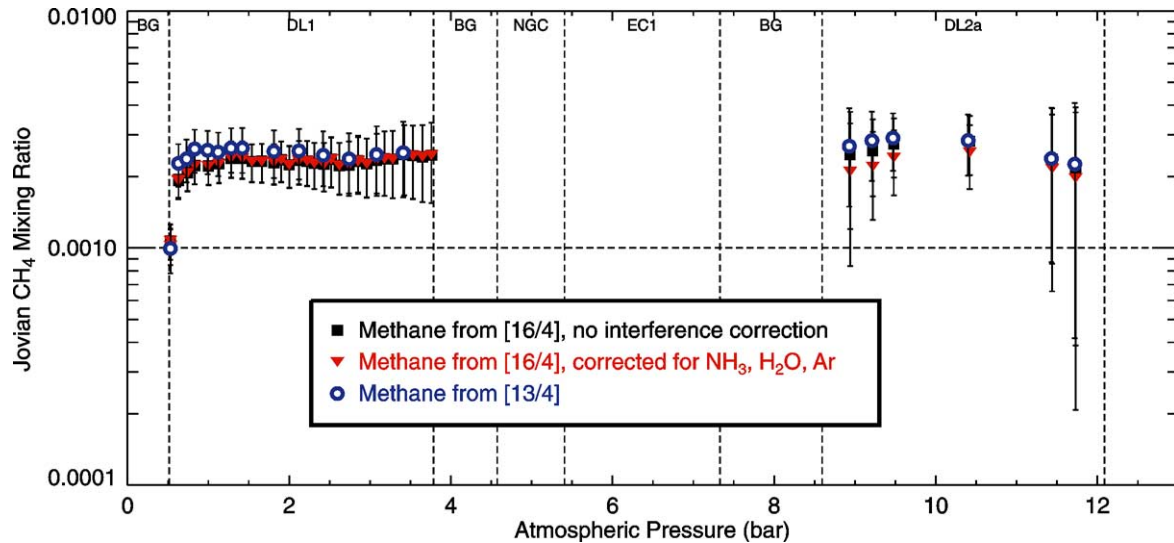


Fig. 9. GPMS CH<sub>4</sub> mixing ratio measurements. The mixing ratio stated in Table 2 is an average of mixing ratios derived from [16/4] (triangles) and [13/4] (circles) in DL1.

Table 2

Deep jovian mixing ratios from GPMS data

Gas	Mixing ratio <sup>a</sup>	Ratio to solar <sup>b</sup>	Comparison to Niemann et al. (1998) <sup>c</sup>
CH <sub>4</sub>	$(2.37 \pm 0.57) \times 10^{-3}$	$3.27 \pm 0.78$	Value increased by 12%. Uncertainty increased by 42%.
NH <sub>3</sub>	$(6.64 \pm 2.54) \times 10^{-4}$	$2.96 \pm 1.13$	Value decreased by 71%. Measurement is no longer an upper limit due to improved background correction.
H <sub>2</sub> S	$(8.9 \pm 2.1) \times 10^{-5}$	$2.75 \pm 0.66$	Value increased by 15%. Uncertainty increased by factor of 4.
H <sub>2</sub> O	$(4.9 \pm 1.6) \times 10^{-4}$	$0.289 \pm 0.096$	Value decreased by 18%. Measurement is no longer an upper limit due to improved background correction.

<sup>a</sup> With respect to hydrogen (Eq. (1)).

<sup>b</sup> Using the solar composition given in Anders and Grevesse (1989).

<sup>c</sup> See text for more details.

### 2.3.2. H<sub>2</sub>S mixing ratio

The H<sub>2</sub>S mixing ratio was observed to increase with pressure throughout DL2a (9–12 bar), reaching a higher value in DL2b ( $p \geq 16$  bar; see Fig. 10). Mixing ratios based on both [34/13] (squares) and [34/4] (triangles) are plotted. The net uncertainties in the DL2a H<sub>2</sub>S mixing ratios are comparable for both series. The [34/13] data suffer from a greater uncertainty in the reference gas (methane) mixing ratio. The [34/4] data have a larger uncertainty due to uncertainty in the deadtime coefficient, since the uncorrected helium reference gas count rate of  $5 \times 10^6$ , compared to the [13] count rate of about  $4 \times 10^5$ , puts the count ratio in a region of greater uncertainty (see Fig. 3). Using the average of H<sub>2</sub>S mixing ratios derived from [34/4] and [34/13], we find that H<sub>2</sub>S in DL2a increases from  $(9.4 \pm 2.2) \times 10^{-6}$  at 8.68 bar to  $(4.8 \pm 1.1) \times 10^{-5}$  at 11.50 bar. In DL2b, deadtime saturation of the helium count rate makes [34/4] very uncertain, so we estimate the H<sub>2</sub>S mixing ratio from the first four [34/13] points and obtain a deep mixing ratio value of  $(8.9 \pm 2.1) \times 10^{-5}$ , or  $(2.75 \pm 0.66) \times$  solar. This estimate is con-

sistent with previously stated GPMS deep H<sub>2</sub>S mixing ratios (Atreya et al., 2003, 1999; Wong et al., 1999; Niemann et al., 1998), but has a larger uncertainty to reflect the more thorough error analysis in this work. Although phosphine makes a contribution to mass 34, the contribution is estimated to be around the 1% level (Wong, 2001) and thus is negligible in view of the stated uncertainties. Since we use methane as a reference gas and derive our deep H<sub>2</sub>S mixing ratio from [34/13], we must assume a value for the jovian methane mixing ratio (see Eqs. (1) and (2)). We used  $w_{\text{CH}_4} = (2.37 \pm 0.57) \times 10^{-3}$  as described above, but readers preferring a different jovian methane mixing ratio should multiply our H<sub>2</sub>S mixing ratio (or the water or ammonia mixing ratios below) by their preferred jovian methane mixing ratio and divide by  $2.37 \times 10^{-3}$  in order to make the correction.

### 2.3.3. Water mixing ratio

GPMS water mixing ratio is plotted in Fig. 11. Given the magnitude of the mixing ratio uncertainties, we cannot reliably determine a change in mixing ratio as a function of

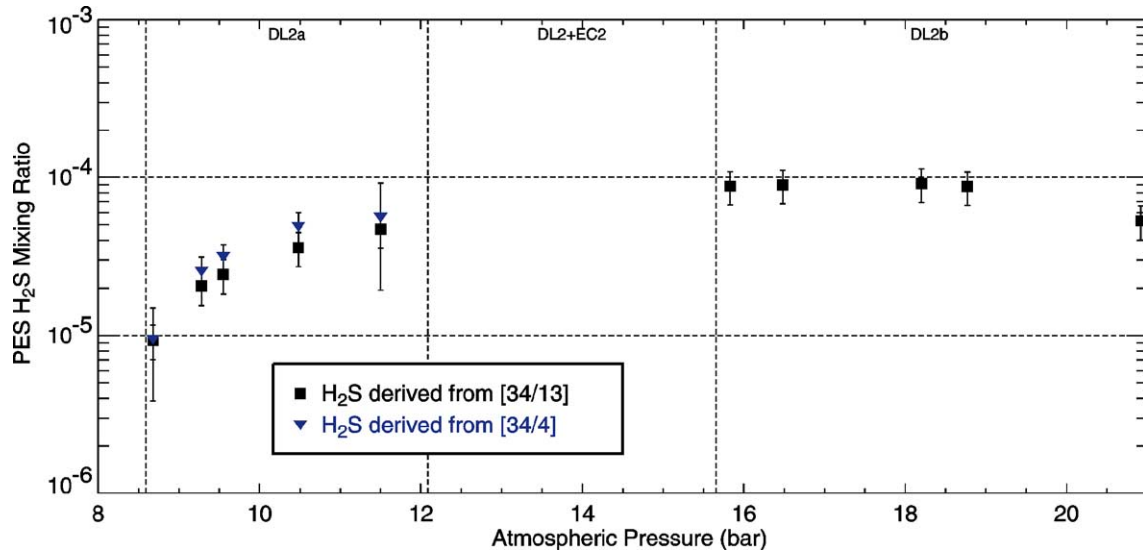


Fig. 10. GPMS H<sub>2</sub>S mixing ratio measurements. Mixing ratios derived from [34/4] (not shown) are unreliable in DL2b, due to saturation of [4] from helium. The last DL2b mixing ratio measurement may suffer from the unanticipated high temperatures encountered by the probe at the end of its descent. The GPMS did not detect H<sub>2</sub>S in DL1.

pressure *within* either the DL2a or DL2b intervals, although we easily conclude that the DL2b mixing ratio is about an order of magnitude greater than the DL2a measurement. Shaded regions in Fig. 11 indicate our water mixing ratios of  $(4.7 \pm 1.5) \times 10^{-5}$  at 11–11.7 bar and  $(4.9 \pm 1.6) \times 10^{-4}$  at 17.6–20.9 bar. Our deep measurement corresponds to an abundance of  $0.29 \pm 0.10$  solar. The current value is about 45% lower than stated in Wong (2001) and Wong and Mahaffy (2001), although still within the stated uncertainty. The pressure dependence of the water calibration constant was the major uncertainty in these previous works, and the current value represents the best determination that can be made with the existing water calibration data. Our current result is also slightly lower than the N98 value of  $(5.6 \pm 2.5) \times 10^{-4}$ , although still consistent with it, since the preliminary N98 result was stated as an upper limit due to the large [18] background residual, which has now been modeled and removed.

#### 2.3.4. Ammonia mixing ratio

The GPMS measurement of [17] is shown in Fig. 12 and is used to derive the ammonia mixing ratio. Mass interference effects from methane, water, and argon (from  $^{36}\text{Ar}^{++}$  at [18]) must be taken into account, as well as the time-varying contribution from ammonia molecules desorbing off the walls of the mass spectrometer. The mass interference correction (the difference between the triangles and circles in Fig. 12) increased with pressure because [18] from water increased over the DL2a pressure range. The decaying residual component (the difference between the triangles and squares in Fig. 12) was described in Section 2.2 and is modeled according to Eq. (9). Then, using the calibration constant shown in Fig. 8, we obtain the ammonia mixing ratio using the [17/13] count ratio. Since the calibration constant and corrected [17] do not vary with pressure, while [13] increases with pressure, Eq. (1) dictates that the resulting

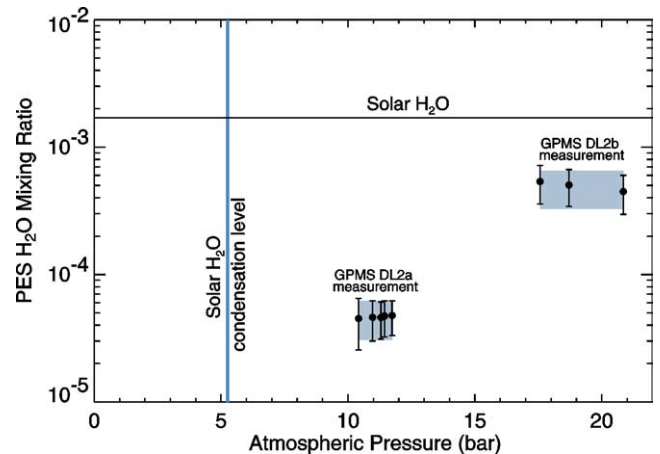


Fig. 11. GPMS H<sub>2</sub>O mixing ratio measurements. Due to the large uncertainty in the water calibration constant, our best recommendation is an average mixing ratio for DL2a, and a second value for DL2b (shaded rectangles). The GPMS did not detect water in DL1.

mixing ratio must decrease with pressure. Thus, we must emphasize that the decrease in the GPMS-derived NH<sub>3</sub> mixing ratio with pressure in Fig. 13 is an artifact of the analysis, and not an actual determination of a pressure variation. Our GPMS analysis provides only an average NH<sub>3</sub> mixing ratio of  $(6.64 \pm 2.54) \times 10^{-4}$  over the 8.9–11.7 bar pressure range of the DL2a ammonia measurements, represented by the shaded rectangle in Fig. 13. This mixing ratio corresponds to a solar enrichment of  $2.96 \pm 1.13$ .

Our NH<sub>3</sub> mixing ratio is consistent with the analysis of the probe-to-orbiter signal attenuation by Folkner et al. (1998) (shown as dataset 3 in Fig. 13), which found a deep ammonia mole fraction of  $700 \pm 100$  ppm, corresponding to a supersolar enrichment of  $3.6 \pm 0.5$  (using the Anders and Grevesse, 1989, nitrogen abundance). The complementary ammonia retrieval from Galileo Probe Net Flux Radiometer

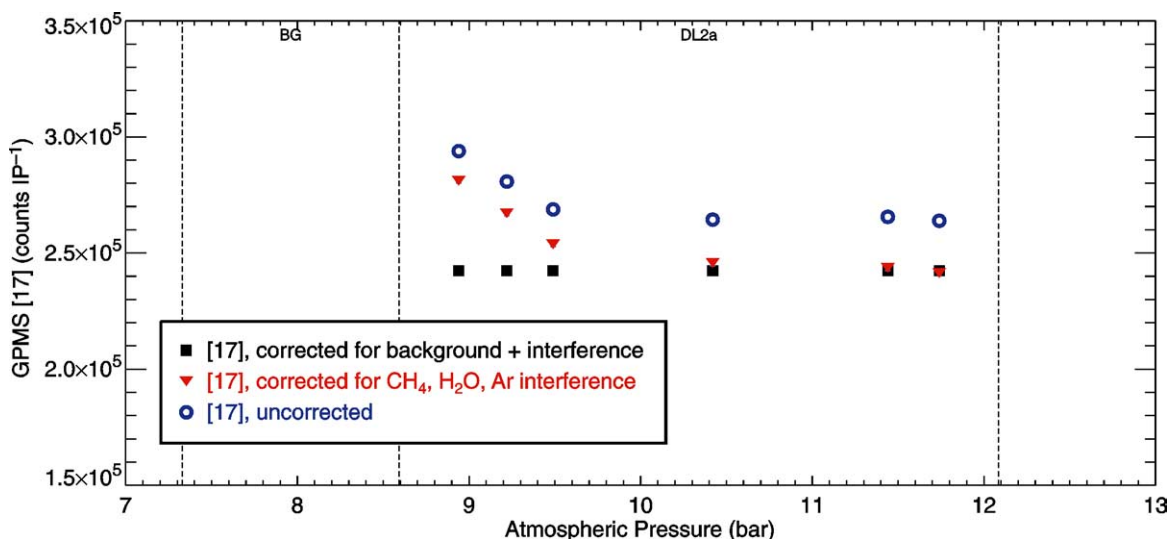


Fig. 12. Counts at  $m/z = 17$  in the DL2a region. Comparison of the triangles and circles shows the relative magnitude of the corrections for mass interference and desorption of  $\text{NH}_3$  from the mass spectrometer interior wall surfaces.

(NFR) data is shown as dataset 2 in Fig. 13 (Sromovsky et al., 1998). Our deep ammonia mixing ratio measurement is not consistent with a solar or subsolar nitrogen abundance in Jupiter's atmosphere. The current analysis supersedes analyses of GPMS [17] presented in previous works (Wong, 2001; Mahaffy et al., 1999; Niemann et al., 1998), which did not utilize the latest calibration and background contribution data presented here.

#### 2.4. Determining the $^{15}\text{N}/^{14}\text{N}$ isotope ratio in $\text{NH}_3$

The  $^{15}\text{N}/^{14}\text{N}$  isotopic ratio in jovian  $\text{NH}_3$  was previously stated in Owen et al. (2001b), and has not been changed for this publication. However, Owen et al. (2001b) did not provide a detailed description of the technique used to determine the isotopic ratio, so we present a full discussion of the analysis here.

The  $^{15}\text{N}/^{14}\text{N}$  ratio was established from the doubly charged  $^{15}\text{NH}_3^{++}/^{14}\text{NH}_3^{++}$  signals. Since the quadrupole analyzer separates ions by their mass to charge ratio, these peaks appear in the mass spectrum at nominal values of 9 and 8.5  $m/z$ , respectively. It was not possible to obtain the  $^{15}\text{N}/^{14}\text{N}$  ratio in  $\text{NH}_3$  using the signal from the singly charged species  $^{15}\text{NH}_3^+$  and  $^{14}\text{NH}_3^+$  at their respective  $m/z$  values of 18 and 17, since the  $\text{H}_2^{16}\text{O}$  contribution to [18] could not be independently constrained. However, during the first enrichment cell experiment (EC1), the ammonia density in the ion source of the mass spectrometer was high enough that the  $^{15}\text{NH}_3^{++}$  signal at  $m/z = 9$  rose to 30 counts  $\text{IP}^{-1}$ . The  $m/z = 8.5$  signal, although not measured directly in this enrichment cell experiment, could be calculated from the knowledge of the  $\text{NH}_3^{++}/\text{NH}_3^+$  ratio produced by the ion source, to yield the  $^{15}\text{NH}_3^{++}/^{14}\text{NH}_3^{++}$  and the  $^{15}\text{N}/^{14}\text{N}$  ratios as described below.

The  $\text{NH}_3^{++}/\text{NH}_3^+$  fragmentation ratio was measured during the Galileo probe descent. This ratio is a general prop-

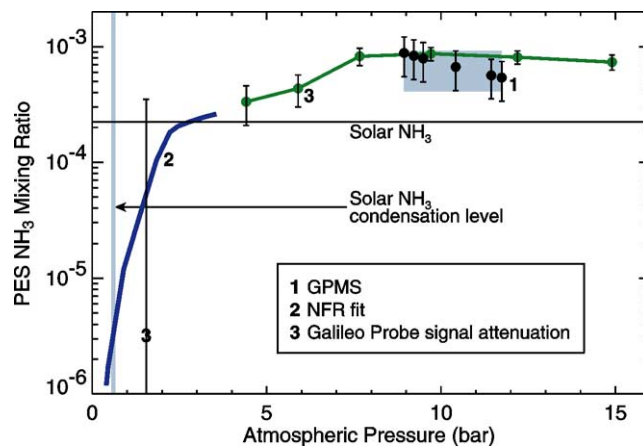


Fig. 13. GPMS  $\text{NH}_3$  mixing ratio (see Section 2.3.4) is compared with NFR (Sromovsky et al., 1998) and probe radio signal (Folkner et al., 1998) retrievals. The decrease in individual GPMS  $\text{NH}_3$  mixing ratio datapoints with increasing pressure is an artifact of the functional form of the background correction (Eq. (9)), so the best GPMS result is an average value for DL2a (shaded rectangle).

erty of the ammonia molecule when bombarded by 75 eV electrons, but it also is affected by individual instrument transmission and detection efficiencies. Generally only the nominal unit mass values for peaks in the 1–150  $m/z$  range were sampled in order to obtain descent profiles for as many species as possible subject to the constraint of the 0.5-sec detector integration period. However, when the probe reached 17.1 bar a high-resolution mass scan sequence was initiated that sampled at 1/8  $m/z$  intervals (Fig. 14). The spectrum was obtained during the Galileo probe descent between pressures of 17.1 and 17.6 bar and shows several doubly charged species in the 6–10  $m/z$  range in addition to numerous singly charged atoms and molecules. This high-resolution scan allowed the  $\text{NH}_3^{++}/\text{NH}_3^+$  ratio to be derived from the portion of [17] due to ammonia and the measurement of [8.5]. The  $\text{NH}_3^{++}/\text{NH}_3^+$  ratio obtained from the descent data is in agree-

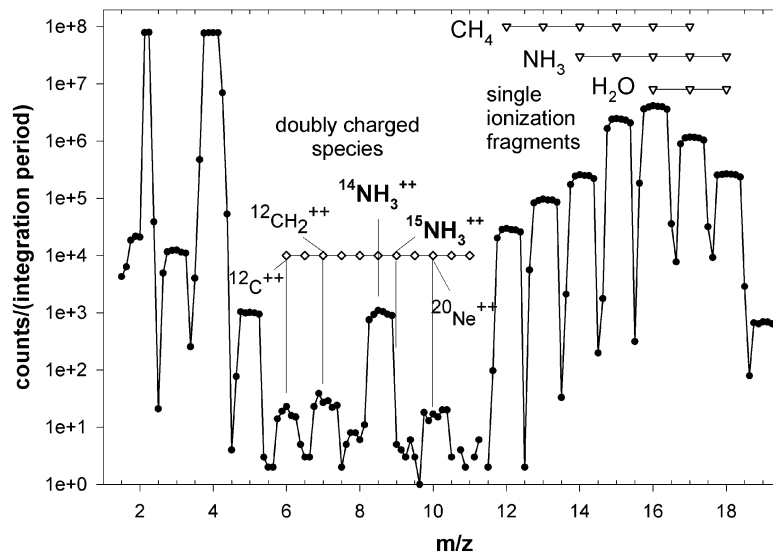


Fig. 14. A 1/8  $m/z$  resolution mass scan obtained near 17 bar in Jupiter's atmosphere features doubly charged species produced by electron impact ionization in the mass spectrometer. This scan gives a value of  $[17/8.5]$  due to  $\text{NH}_3^+/\text{NH}_3^{++}$  of about 1000, which is used to determine the  $^{15}\text{N}/^{14}\text{N}$  isotopic ratio as described in Section 2.4.

ment with the ratio obtained in subsequent studies using the EU. Calibration data from both pre-launch FU studies and post encounter EU calibration studies also allowed the fragmentation patterns of water, ammonia, argon and methane to be obtained so that the methane and water contributions could be removed from [17] (see Fig. 4). The  $\text{Ar}^{++}/\text{Ar}^+$  ratio is needed to remove the  $^{36}\text{Ar}^{++}$  contribution from the observed [18], based on the [36] signal dominated by  $^{36}\text{Ar}^+$ . Calibration runs on the EU furthermore allowed us to establish that the relative contributions of water or methane to both [8.5] and [9.0] are totally negligible, and that  $^{15}\text{NH}_3^{++}$  and  $^{14}\text{NH}_3^{++}$  indeed dominate the contribution to the signal at these mass values. EU studies also confirm that the  $[9]/[8.5]$  ratio from  $\text{NH}_3^{++}$  gives an accurate measurement of (terrestrial)  $^{15}\text{N}/^{14}\text{N}$ .

Despite its usefulness in determining the  $\text{NH}_3^{++}/\text{NH}_3^+$  ratio, the single [8.5] data point, together with the [9.0] data point taken several integration periods later during this high resolution scan, cannot accurately establish the  $^{15}\text{NH}_3/^{14}\text{NH}_3$  ratio, due to the very large statistical count rate uncertainty associated with the measured value of  $[9.0] = 5$  counts  $\text{IP}^{-1}$ . However, the three measurements of [9.0] in EC1 are sufficiently high to reduce statistical counting errors and allow us to calculate the  $^{15}\text{N}/^{14}\text{N}$  ratio in  $\text{NH}_3$ . Measured or calculated count values in the enrichment cell experiment and the resulting  $[9]/[8.5]$  ratio are shown in Fig. 15. Since [9] is still low and there are only three data points, the errors are dominated by the statistical count uncertainty. The data shown in Fig. 15 lead to our result of  $^{15}\text{N}/^{14}\text{N} = (2.3 \pm 0.3) \times 10^{-3}$ .

### 3. Discussion

Knowledge of Jupiter's condensible volatiles addresses two key problems—the formation of Jupiter, and the me-

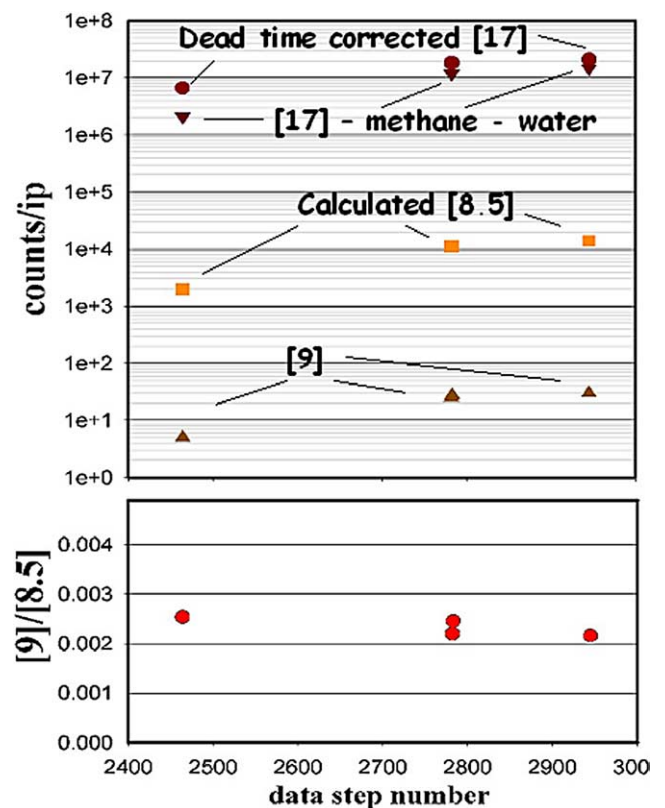


Fig. 15. Enrichment Cell 1 (see Fig. 1) measurements of [17] and [9] are shown as a function of sequence step number (top panel). The measurement of  $[17/8.5]$  from Fig. 14 is used to estimate [8.5] based on measured [17] in EC1, and the resulting  $[9/8.5]$  (bottom panel) yields the  $^{15}\text{N}/^{14}\text{N}$  result of  $(2.3 \pm 0.3) \times 10^{-3}$ .

teology of its troposphere. The jovian nitrogen isotope ratio may provide the best current estimate of the protosolar  $^{15}\text{N}/^{14}\text{N}$  ratio, although a more precise direct measurement from the solar wind may be realized with the return

of the Genesis samples (Burnett et al., 2003). This ratio is important for studies of loss mechanisms of planetary atmospheres. Deep, well-mixed condensible volatile mixing ratios are also used to constrain models of planetary formation, and the GPMS data provides the only measurement of the deep H<sub>2</sub>S mixing ratio. Our methane and ammonia mixing ratios confirm the supersolar values obtained from remote sensing studies, but the water measurement does not establish the deep water mixing ratio due to local meteorology. The observed variation of condensible volatile mixing ratios with depth was largely unexpected, and explaining the staggered recovery levels—the depths at which the condensible volatiles reach their well-mixed abundances and subsequently maintain constant mixing ratios with increasing pressure—is an important criterion for models ranging in scope from 5- $\mu$ m hotspots to the north equatorial belt, and possibly to the entire jovian troposphere.

### 3.1. Composition

The <sup>15</sup>N/<sup>14</sup>N ratio in jovian NH<sub>3</sub> of  $(2.3 \pm 0.3) \times 10^{-3}$  given by the analysis of Section 2.4 has been discussed (Owen et al., 2001a, 2001b). Since this result is consistent with the recent ISO Jupiter measurement of  $1.9^{+0.9}_{-1.0} \times 10^{-3}$  (Fouchet et al., 2000) there is no longer reason to believe that the terrestrial value of  $3.66 \times 10^{-3}$  should be accepted as the protosolar value. This determination has received further confirmation from analyses of infrared spectra of Jupiter obtained by the CIRS instrument during the Cassini flyby of Jupiter in December 2000; Abbas et al. (2004) found <sup>15</sup>N/<sup>14</sup>N =  $(2.23 \pm 0.31) \times 10^{-3}$  while Fouchet et al. (2004) derived a value of  $(2.2 \pm 0.5) \times 10^{-3}$  for this ratio. The GPMS measurement, based on gas sampled near 2 bar, is a deeper result than remote sensing measurements, and is therefore unaffected by the possibility that nitrogen might be fractionated during cloud condensation (Fouchet et al., 2000). Although it is difficult to measure this ratio precisely in the solar wind itself (Kallenbach et al., 1998) or to isolate the solar wind component of nitrogen from measurements on returned lunar grains (Kerridge and Marti, 2001), recent detailed studies of near surface regions of individual lunar grains (Hashizume et al., 2000) are consistent with the jovian results. Although further direct solar wind measurements and the Genesis samples will be of value to resolve the discrepancy between the difficult lunar grain experiments, we suggest that it is likely that the protosolar <sup>15</sup>N/<sup>14</sup>N ratio is considerably lower than that of any of the terrestrial planets, and that the jovian atmosphere retains an accurate signature of the protosolar value.

The abundances of the volatile elements carbon, oxygen, nitrogen, and sulfur provide valuable insight into both the formation of the planet as well as into conditions of the early solar nebula. The core accretion model of gas giant formation (e.g., Perri and Cameron, 1974; Mizuno et al., 1978; Podolak et al., 1993), in which planetesimals accrete onto a dense protoplanetary core until the core gains enough mass

to capture gas directly from the protosolar nebula, is supported by the supersolar enrichments of volatile elements indicated by Table 2, since both outgassing from the core and accretion of additional planetesimals into the gaseous envelope would act to enrich the planet in condensed volatiles. In particular, the nearly solar C/S ratio on Jupiter has led to the suggestion (Owen et al., 1997; Anders and Grevesse, 1989) that the accreted planetesimals were icy rather than rocky. However, the nearly solar C/N ratio is more difficult to justify, because we know of no solid planetesimals with this ratio. The GPMS NH<sub>3</sub> mixing ratio measurement provides an important independent confirmation of the nearly solar C/N ratio in Jupiter derived from analysis of radio data, helping to allay concerns (de Pater et al., 2001; Folkner et al., 1998; Atreya et al., 1999) that other gaseous microwave absorbers in Jupiter's atmosphere could lead to overestimation of the ammonia fraction as derived from attenuation of the probe's radio signal.

At Jupiter's distance from the Sun in the protosolar nebula, the primary reservoir of nitrogen should have been gaseous N<sub>2</sub>. Then according to the core accretion model, Jupiter's nitrogen should have been largely obtained through direct gas accretion, resulting in a more nearly solar N/H ratio and a supersolar C/N ratio, if the accreted planetesimals were depleted in nitrogen as is apparently the case for some comets (Cochran et al., 2000). Jupiter's high nitrogen abundance in the framework of this model implies that significant nitrogen was present in the solid phase, i.e., trapped in water ice. It has been suggested that one way to realize this is by formation of the icy planetesimals accreted by proto-Jupiter at very low temperatures ( $T < 40$  K), since only at these temperatures can N<sub>2</sub> be trapped in water ice (Bar-Nun et al., 1988; Gautier et al., 2001). The scenario of Owen et al. (1999) maintains consistency with the observed solar C/N ratio by suggesting that Jupiter could have been enriched by cold icy planetesimals brought in from the Kuiper belt, or even from the collapsing interstellar cloud that formed the solar nebula. Another suggestion is that Jupiter began its formation after the solar nebula had cooled down below 40 K at 5 AU (Gautier et al., 2001). On the other hand, the recent discovery (Sigurdsson et al., 2003) of an ancient Jupiter-sized planetary companion to the pulsar B1620-26 in its low metallicity globular cluster may provide an example of planetary formation by mechanisms other than the core instability model, since systems formed in low metallicity environments are not expected to have had sufficient condensed material to form a large enough core and trigger runaway gas accretion.

### 3.2. Meteorology

The PES was the one location on Jupiter where mixing ratio profiles of all three condensible volatiles were constrained (down to pressures of about 20 bar). Although it is disappointing that the deep, well-mixed water mixing ratio was not observed, the pressure-variation of the conden-

sible volatiles (as tracers of atmospheric motion) provides valuable insights into the weather in Jupiter's troposphere. Our findings are consistent with the idea that processes other than condensation act in Jupiter's atmosphere to reduce concentrations of the condensible volatiles, an idea that has been suggested to explain dryness in the probe entry site (Atreya et al., 1996, 1997; Owen et al., 1997; Showman and Ingersoll, 1998; Baker and Schubert, 1998; Friedson and Orton, 1999; Showman and Dowling, 2000). Even outside the PES, remote sensing has revealed substantially subsaturated mixing ratios of ammonia from spectra at centimeter wavelengths, in both global and zonally averaged (e.g., de Pater and Dickel, 1986) and latitudinally resolved (Sault et al., 2004) measurements. Low water mixing ratios have also been derived from infrared data (e.g., Bjoraker et al., 1986). Depletion of water is supported by the failure to detect the water cloud base in NIMS observations (Roos-Serote et al., 2004), but other cloud studies contradict the picture of Jupiter as a dry planet: there is fairly even cloud coverage near 750 mbar (presumably from ammonia ice; Banfield et al., 1998) and near 2 bar (presumably  $\text{NH}_4\text{SH}$ ; e.g., Roos-Serote et al., 1999; Nixon et al., 2001).

Ammonia is the best-studied of Jupiter's condensible volatiles, because of its wealth of spectral features in most wavelength regions as well as its low condensation temperature. Analysis of Jupiter's microwave emission (de Pater et al., 2001) indicates widespread ammonia depletion, with ammonia mixing ratios decreasing with altitude at  $p < 4$  bar, and with about  $0.5 \times$  solar ammonia at  $p \leq 2$  bar. Since the lifting condensation level for  $3 \times$  solar ammonia is near 1 bar, these ammonia results imply depletion of ammonia through a process other than (or in addition to) the condensation of ammonia ice. The microwave data were longitudinally averaged, but Sault et al. (2004) were able to remove the rotational smearing and retrieve longitudinally resolved maps of Jupiter's thermal microwave emission at 2 cm. Although they found variation in both latitude and longitude, both warm and cold areas showed the deep depletion of ammonia gas. But in Galileo SSI near-infrared data, the uppermost cloud layer is observed to have a largely constant cloud base on a planet-wide scale, at  $750 \pm 250$  mbar (Banfield et al., 1998). Since the retrieved pressures indeed correspond to cloud bases instead of cloud tops, they can be compared to cloud base pressures calculated by the equilibrium cloud condensation model: 750 mbar for a  $2 \times$  solar enrichment and 1 bar for  $3 \times$  solar enrichment of ammonia. Thus, cloud base retrievals are consistent with the deep ammonia enrichments of  $2.96 \pm 1.13 \times$  solar from GPMS data (Section 2.3.4), and nearly consistent with the  $3.6 \times$  solar based on attenuation of the probe-to-orbiter signal (Folkner et al., 1998). This finding is puzzling because the lifting condensation level for  $0.5 \times$  solar ammonia is around 600 mbar, a somewhat lower pressure than derived by Banfield et al. (1998) for the average cloud base. Even so, the lifting condensation level for the depleted ammonia gas profile derived

from radio observations is within the limits stated in Banfield et al. (1998).

The elusive sulfur-containing cloud layer has not been directly observed, but indirect evidence for its existence abounds. Perhaps the strongest indication of the  $\text{NH}_4\text{SH}$  cloud is the lack of signatures of  $\text{H}_2\text{S}$  in disk-averaged spectra of Jupiter in the near-IR (Larson et al., 1984). Presuming that the GPMS measurement of around three times solar  $\text{H}_2\text{S}$  at pressures greater than 16 bar in the PES gives the deep abundance of  $\text{H}_2\text{S}$ , the lack of  $\text{H}_2\text{S}$  seen planet-wide at higher altitudes indicates a loss process for  $\text{H}_2\text{S}$  on a global scale, and condensation of a nitrogen-sulfur compound such as  $\text{NH}_4\text{SH}$  is the most obvious mechanism (Lewis, 1969; Weidenschilling and Lewis, 1973; Atreya and Romani, 1985). The direct condensation of  $\text{H}_2\text{S}$  is ruled out because temperatures are only low enough for  $\text{H}_2\text{S}$  condensation near the tropopause, and  $\text{H}_2\text{S}$  clouds at that level would be clearly visible. Radiative models used to calculate 5- $\mu\text{m}$  emission from Jupiter also rely on the presence of a cloud at about 2 bar (e.g., Roos-Serote et al., 1999; Nixon et al., 2001). Although most of the 5- $\mu\text{m}$  emission originates at pressures of 1 to 5 bar (depending on wavelength; see, e.g., Nixon et al., 2001), the major source of opacity at this wavelength is the 2-bar cloud. Reduced cloud opacity results in 5- $\mu\text{m}$  brightening, as is seen in hot spots such as the one that encompassed the PES. Since the GPMS measurement of the  $\text{H}_2\text{S}$  mixing ratio profile in the peculiar PES is the only measurement of  $\text{H}_2\text{S}$  in Jupiter, it is unknown whether there is a problematic discrepancy between  $\text{H}_2\text{S}$  mixing ratio and the 2-bar cloud level, as there seems to be with the  $\text{NH}_3$  mixing ratio and the ammonia cloud. In fact, Romani et al. (2000) and de Pater et al. (2001) suggested that the sulfur-containing 2-bar cloud layer might have a greater efficiency at removing gaseous ammonia from Jupiter's atmosphere than previously thought, thereby explaining the widespread depletion of  $\text{NH}_3$  gas deeper than its condensation level.

Retrievals of water mixing ratio from 5- $\mu\text{m}$  Voyager IRIS and Kuiper Airborne Observatory observations (Bjoraker et al., 1986; Drossart and Encrenaz, 1982; Lellouch et al., 1989) are consistent with subsaturated water at the pressure levels predicted to hold the water cloud. However, these observations suffer from low spatial resolution and are strongly weighted towards regions that are bright at 5  $\mu\text{m}$ . This bias makes it difficult to make inferences about Jupiter's overall water vapor distribution, but at the very least the observations suggest that the depletion of water seen in the probe entry site is not unique. However, there is a crucial distinction between the pressure levels of remote-sensing and GPMS water mixing ratio determinations: 5- $\mu\text{m}$  observations are sensitive to pressures of about 5 bar or less (but still within the expected pressure levels of the water cloud), whereas the GPMS returned water mixing ratios between 11 and 21 bar (much deeper than the expected cloud base). Thus, the GPMS measurement indicates a severe depletion

of water to much greater depths than the depletion previously noted in 5- $\mu\text{m}$  data.

For an adiabatically uplifted parcel of air containing  $\text{H}_2\text{O}$  in solar abundance, a cloud would form at approximately the 5-bar level (Weidenschilling and Lewis, 1973; Atreya et al., 1999). Roos-Serote et al. (2004) modeled 5- $\mu\text{m}$  NIMS spectra of Jupiter, finding (1) subsaturated water in all spectra analyzed, and (2) no significant cloud opacity at pressures between 2.5 bar and 5 bar. Although they could satisfactorily match the NIMS spectra with models having no water cloud opacity at all, their favored spectral models had cloud tops deeper than 5 bar, and therefore cloud bases even deeper than this. A water condensation level at  $p > 5$  bar requires supersolar water. Ingersoll and Kanamori (1995) modeled atmospheric waves from SL9 impacts as gravity waves trapped between the tropopause and a deeper stable layer. This stable layer was assumed to be the base of the water cloud, and the calculated depth of 12 bar corresponds to an approximate supersolar enrichment of water by a factor of 10, although no other observation has been able to support such an extreme enrichment.

Water clouds have been observed at isolated sites on Jupiter by Galileo SSI measurements (Gierasch et al., 2000; Simon-Miller et al., 2000), but these features have been recognized as convective thunderstorm cloud tops. Without identifying the cloud base, water cloud observations cannot constrain the deep water abundances. Dyudina et al. (2002) analyzed the optical power of lightning detected in the  $\text{H}_\alpha$  line in Galileo SSI images finding that the lower power observed is consistent with lightning generated at  $p > 5$  bar. Lightning production at such great depths implies a supersolar water abundance. Although observations of water ice at the visible cloud tops (Gierasch et al., 2000) and lightning on Jupiter (Smith et al., 1979; Borucki et al., 1982; Little et al., 1999; Dyudina et al., 2002) indicate the presence of convective water clouds, the observations are consistent with relatively rare, localized convective events. Observed lightning events are limited to regions of the planet with cyclonic shear, and near the centers of westward jets (Little et al., 1999).

Two mechanisms have been suggested to explain the deep depletion of condensible volatiles in the probe entry site: the entraining downdraft hypothesis (Atreya et al., 1996; Showman and Ingersoll, 1998; Wong et al., 1998; Hueso et al., 1999) and the column stretching hypothesis (Showman and Ingersoll, 1998; Friedson and Orton, 1999; Showman and Dowling, 2000). For both scenarios, the initial state of the atmosphere must have condensible volatile mixing ratios that increase with depth, although there is no requirement that the condensible volatile profiles match those in the equilibrium cloud condensation model (ECCM), in which condensible volatiles are well mixed at depth, with condensation-limited mixing ratios above the cloud bases. Column stretching explains condensible volatile depletion in terms of Rossby wave models such as those of Showman and Dowling (2000) and Friedson and Orton (1999) (schematic

diagram also reproduced Baines et al., 2002). In this scenario the atmospheric column is stretched vertically, so that levels with low condensible volatile mixing ratios are shifted down to higher pressures. In the entraining downdraft model, a parcel at the top of the atmosphere, dried of its condensible volatiles, moves downwards and entrains (laterally mixes with) surrounding air during its descent. The entrainment of surrounding air is responsible for the gradual increase in condensible volatile mixing ratios with pressure. The downdraft model of Hueso et al. (1999) was unable to match the PES condensible volatile profiles because they used environmental mixing ratio profiles based on the equilibrium cloud condensation model. Wong (2001) found that no entraining downdraft model could duplicate PES condensible volatile profiles if the surrounding atmosphere from which air is entrained is as described by the equilibrium cloud condensation model. Entraining downdraft model runs that were able to match the mixing ratio profile of a single condensible volatile (e.g.,  $\text{NH}_3$ ) were unable to simultaneously match the profiles of the other two condensible volatiles (e.g.,  $\text{H}_2\text{S}$  and  $\text{H}_2\text{O}$ ). This finding is independent of the vertical coordinate used (altitude, pressure, or potential temperature) and depends only on the ratios of condensible volatiles to each other at a given altitude. Qualitatively, it was found that if a deep depletion down to a well-mixed equilibration level was produced in one condensible volatile profile, then all three condensible volatiles would have approximately the same equilibration level, since the entrainment rate was the dominant factor in shaping the mixing ratio profiles in the downdraft.

If column stretching is used to explain the PES condensible volatile profiles, then a quantitative look at the mixing ratios of the three condensible volatiles shows that the original pre-stretched column did not feature condensation-limited (ECCM-type) condensible volatile profiles. The relative concentrations of the three condensible volatiles at each level in the pre-stretched column would be preserved via stretching, and the PES condensible volatile profiles feature relative mixing ratios that never occur in an ECCM column. For instance, the condensation-limited  $\text{H}_2\text{S}$  mole fraction at the ammonia cloud base should be  $1.3 \times 10^{-12}$ . After stretching the ammonia cloud base level down to the ammonia equilibration level of 8 bar in the PES,  $\text{H}_2\text{S}$  should remain on the order of  $10^{-12}$ . However, extrapolation of the  $\text{H}_2\text{S}$  mixing ratio in that pressure region in the PES leads to values between  $10^{-6}$  and  $10^{-5}$ , with the closest GPMS measurement being  $(8.4 \pm 3.6) \times 10^{-6}$  at 8.68 bar, about a million times greater than mole fractions that would be expected for stretching of an ECCM column. Although the ECCM is a simple one-dimensional model, its basic thermodynamic conclusion is compelling: at the temperature where  $\text{NH}_3$  ice condenses, the  $\text{H}_2\text{S}$  mole fraction is condensation-limited (by equilibrium with condensed  $\text{NH}_4\text{SH}$ ) such that  $n_{\text{H}_2\text{S}}/n_{\text{NH}_3} \approx 2 \times 10^{-9}$ . The PES value of  $n_{\text{H}_2\text{S}}/n_{\text{NH}_3} \approx 2 \times 10^{-3}$  therefore implies that the ammonia equilibration level sensed by the Galileo probe is not a column-stretched

relic of the ammonia cloud base, since such high abundances of H<sub>2</sub>S could not exist at the ammonia cloud base. Likewise, the water mixing ratio is one to two orders of magnitude too large at the H<sub>2</sub>S equilibration level. Thus, if column stretching has occurred in the PES, then the original column must have had reduced ammonia and reduced H<sub>2</sub>S at the respective equilibrium condensation levels predicted by the deep mixing ratios of these gases.

But Jupiter's condensible volatiles may be more than passive tracers of atmospheric motion—they may actually help govern the motion. Platten and Legros (1984) note that “any system, in which the fluid density depends on two variables that diffuse at different rates, may exhibit unexpected convection.” The jovian atmosphere is just such a system: its internal heat flux is the destabilizing force driving convection, while the decrease with altitude of condensible volatile abundances (with water being the most influential) provides a stabilizing molecular weight gradient. In the jovian two-dimensional fluid dynamical model of Nakajima et al. (2000), the stable layer created at the water lifting condensation level (LCL) established a compositional and dynamic boundary. Below their water LCL of 5 bar, vigorous convection occurred and the water mixing ratio was homogeneous, featuring regularly distributed deep convective cells that did not extend above the stable layer. Guillot (1995) also claimed that for water abundances of more than  $4.6 \times$  solar, molecular weight stratification on Jupiter would be so strong as to generally inhibit convection. The situation is qualitatively similar to double diffusive systems like the experiment of Turner (1968), in which heat is applied to the bottom of a tank of water with a stable salinity gradient: a fluid parcel experiencing a small vertical displacement oscillates vertically due to the restoring buoyancy force imposed by the compositional gradient, leading to the growth of a well-mixed convective layer with a stable top boundary characterized by a step in solute density. According to Guillot (1995) and Stevenson (1979), the small value of the relevant Prandtl number on Jupiter (the ratio of the kinematic viscosity to the radiative diffusivity) is too low for diffusive layer boundaries to persist, so that layered convection would not occur. Furthermore, Guillot (1995) concluded that the oscillations involved in diffusive convective motion “should dry out the atmosphere substantially below the saturation level,” a suggestion that may explain the stable layer at 12 bar inferred by Ingersoll and Kanamori (1995).

Jupiter does experience free convection at discrete locations, based on the detection of convective storm clouds (Gierasch et al., 2000) and lightning (Little et al., 1999). In these convective areas condensible volatile mixing ratios should be as predicted by equilibrium cloud condensation models. On the other hand, we have used the vertical mixing ratio profiles of the condensible volatiles to show that in both the PES and the regions around it, mechanisms other than condensation influence the concentrations of these gases. Molecular stratification and double diffusive effects, as suggested by Guillot (1995), may be significant. Numerous in-

frared and radio remote sensing studies are also consistent with ammonia and water vertical profiles being depleted, over a substantial portion of the planet, with respect to the simple equilibrium cloud condensation model. Our understanding of the nature of convection on Jupiter could best be enhanced by increasing the data available on the vertical gradients of temperature and condensible volatiles at multiple positions on the planet.

## Acknowledgments

This work was supported by the Galileo project through the NASA GSRP and by a NASA Planetary Atmospheres grant to S.K.A., and partially performed while M.H.W. held a National Research Council Research Associateship Award at NASA Goddard Space Flight Center. We thank Adam Showman for helpful discussions and a constructive review and Peter H. Wong for research assistance.

## References

- Abbas, M.M., LeClair, A., Owen, T., Conrath, B.J., Flasar, F.M., Kunde, V.G., Nixon, C.A., Achterberg, R.K., Bjoraker, G., Jennings, D.J., Orton, G., Romani, P.N., 2004. The nitrogen isotopic ratio in Jupiter's atmosphere from observations by the Composite Infrared Spectrometer on the Cassini spacecraft. *Astrophys. J.* 602, 1063–1074.
- Anders, E., Grevesse, N., 1989. Abundances of the elements—meteoritic and solar. *Geochim. Cosmochim. Acta* 53, 197–214.
- Atreya, S.K., Romani, P.N., 1985. Photochemistry and clouds of Jupiter, Saturn and Uranus. In: Hunt, G.E. (Ed.), *Recent Advances in Planetary Meteorology*. Cambridge Univ. Press, New York, pp. 17–68.
- Atreya, S.K., Owen, T.O., Wong, M.H., 1996. Condensible volatiles, clouds, and implications for meteorology in the Galileo probe entry region: Jupiter is not dry! *Bull. Am. Astron. Soc.* 28, 1133–1134.
- Atreya, S.K., Wong, M.H., Owen, T.C., Niemann, H.B., Mahaffy, P.R., 1997. Chemistry and clouds of the atmosphere of Jupiter: a Galileo perspective. In: Barbieri, C., Rahe, J.H., Johnson, T.V., Sohus, A.M. (Eds.), *Three Galileos: The Man, The Spacecraft, The Telescope*. Kluwer Academic, Dordrecht, The Netherlands, pp. 249–260.
- Atreya, S.K., Wong, M.H., Owen, T.O., Mahaffy, P.R., Niemann, H.B., de Pater, I., Drossart, P., Encrenaz, Th., 1999. A comparison of the atmospheres of Jupiter and Saturn: deep atmospheric composition, cloud structure, vertical mixing, and origin. *Planet. Space Sci.* 47, 1243–1262.
- Atreya, S.K., Mahaffy, P.R., Niemann, H.B., Wong, M.H., Owen, T.C., 2003. Composition of the atmosphere of Jupiter—an update, and implications for the extrasolar giant planets. *Planet. Space Sci.* 51, 105–112.
- Baker, R.D., Schubert, G., 1998. Deep convective entrainment by downdrafts in Jupiter's atmosphere. *Icarus* 136, 340–343.
- Baines, K.H., Carlson, R.W., Kamp, L.W., 2002. Fresh ammonia ice clouds in Jupiter. *Icarus* 159, 74–94.
- Banfield, D., Gierasch, P.J., Bell, M., Ustinov, E., Ingersoll, A.P., Vasavada, A.R., West, R.A., Belton, M.J.S., 1998. Jupiter's cloud structure from Galileo imaging data. *Icarus* 135, 230–250.
- Bar-Nun, A., Kleinfeld, I., Kochavi, E., 1988. Trapping of gas mixtures by amorphous water ice. *Phys. Rev. B* 38, 7749–7754.
- Bevington, P.R., Robinson, D.K., 1992. *Data Reduction and Error Analysis for the Physical Sciences*. WCB/McGraw-Hill, Dubuque, IA.
- Bjoraker, G.L., Larson, H.P., Kunde, V.G., 1986. The abundance and distribution of water vapor in Jupiter's atmosphere. *Astrophys. J.* 311, 1058–1072.

- Borucki, W.J., Bar-Nun, A., Scarf, F.L., Cook II, A.F., Hunt, G.E., 1982. Lightning activity on Jupiter. *Icarus* 52, 492–502.
- Burnett, D.S., Barraclough, B.L., Bennett, R., Neugebauer, M., Oldham, L.P., Sasaki, C.N., Sevilla, D., Smith, N., Stansbery, E., Sweetnam, D., Wiens, R.C., 2003. The Genesis Discovery Mission: return of solar matter to Earth. *Space Sci. Rev.* 105 (3), 509–534.
- Cochran, A.L., Cochran, W.D., Barker, E.S., 2000.  $N_2^+$  and  $CO^+$  in Comets 122P/1995 S1 (deVico) and C/1995 O1 (Hale-Bopp). *Icarus* 146, 583–593.
- de Pater, I., Dickel, J.R., 1986. Jupiter's zone-belt structure at radio wavelengths. I. Observations. *Astrophys. J.* 308 (1), 459–471.
- de Pater, I., Dunn, D., Romani, P.N., Zahnle, K., 2001. Reconciling Galileo probe data and ground-based radio observations of ammonia on Jupiter. *Icarus* 149, 66–78.
- Drossart, P., Encrenaz, Th., 1982. The abundance of water on Jupiter from the Voyager IRIS data at 5 micron. *Icarus* 52, 483–491.
- Dyudina, U.A., Ingersoll, A.P., Vasavada, A.R., Ewald, S.P., the Galileo SSI Team, 2002. Monte Carlo radiative transfer modeling of lightning observed in Galileo images of Jupiter. *Icarus* 160, 336–349.
- Folkner, W.M., Woo, R., Nandi, S., 1998. Ammonia abundance in Jupiter's atmosphere derived from attenuation of the Galileo probe's radio signal. *J. Geophys. Res.* 103, 22847–22856.
- Fouchet, T., Lellouch, E., Bézard, B., Encrenaz, Th., Drossart, P., Feuchtergruber, H., de Graauw, T., 2000. ISO-SWS observations of Jupiter: measurement of the ammonia tropospheric profile and of the  $^{15}N/^{14}N$  isotopic ratio. *Icarus* 143, 223–243.
- Fouchet, T., Irwin, P.G.J., Parrish, P., Calcutt, S.B., Taylor, F.W., Nixon, C.A., Owen, T.C., 2004. Search for spatial variation in the jovian  $^{15}N/^{14}N$  ratio from Cassini/CIRS observations. *Icarus*. In press.
- Friedson, A.J., Orton, G.S., 1999. A dynamical model of Jupiter's 5-micron hot spots. *Bull. Am. Astron. Soc.* 31, 1155–1156.
- Gautier, D., Bézard, B., Marten, A., Baluteau, J.P., Scott, N., Chedin, A., Kunde, V., Hanel, R., 1982. The C/H ratio in Jupiter from the Voyager infrared investigation. *Astrophys. J.* 257, 901–912.
- Gautier, D., Hersant, F., Mousis, O., Lunine, J.I., 2001. Enrichments in volatiles in Jupiter: a new interpretation of the Galileo measurements. *Astrophys. J.* 550 (2), L227–L230.
- Gierasch, P.J., Ingersoll, A.P., Banfield, D., Ewald, S.P., Helfenstein, P., Simon-Miller, A., Vasavada, A., Breneman, H.H., Senske, D.A., the Galileo Imaging Team, 2000. Observation of moist convection in Jupiter's atmosphere. *Nature* 403, 628–630.
- Guillot, T., 1995. Condensation of methane, ammonia, and water and the inhibition of convection in giant planets. *Science* 269, 1697–1699.
- Hashizume, K., Chaussidon, M., Marty, B., Robert, F., 2000. Solar wind record on the Moon: deciphering presolar from planetary nitrogen. *Science* 290, 1142–1145.
- Hueso, R., Sánchez-Lavega, A., Drossart, P., 1999. A theoretical study of parcel stability and cloud distribution in a jovian hot spot. *Planet. Space Sci.* 47, 1263–1275.
- Ingersoll, A.P., Kanamori, H., 1995. Waves from the collisions of Comet Shoemaker–Levy 9 with Jupiter. *Nature* 374 (6524), 706–708.
- Kallenbach, R., Geiss, J., Ipavich, F.M., Gloeckler, G., Bochsler, P., Gliem, F., Hefiti, S., Hilchenbach, M., Hovestadt, D., 1998. Isotopic composition of solar wind nitrogen: first in situ determination with the CELIAS/MTOF spectrometer on board SOHO. *Astrophys. J.* 507, L185–L188.
- Kerridge, J.F., Marti, K., 2001. Solar nitrogen measurements and records of past radiations. In: *Annual Lunar and Planetary Science Conference*, 32nd, March 12–16. Houston TX. Abstract 1246.
- Knacke, R.F., Kim, S.J., Ridgway, S.T., Tokunaga, A.T., 1982. The abundances of  $CH_4$ ,  $CH_3D$ ,  $NH_3$ , and  $PH_3$  in the troposphere of Jupiter derived from high-resolution  $1100\text{--}1200\text{ cm}^{-1}$  spectra. *Astrophys. J.* 262, 388–395.
- Larson, H.P., Davis, D.S., Hoffman, R., Bjoraker, G., 1984. The jovian atmospheric window at  $2.7\text{ }\mu\text{m}$ : a search for  $H_2S$ . *Icarus* 60, 621–639.
- Lellouch, E., Drossart, P., Encrenaz, Th., 1989. A new analysis of the jovian 5-micron Voyager/IRIS spectra. *Icarus* 77, 457–465.
- Lewis, J.S., 1969. The clouds of Jupiter and the  $NH_3\text{--}H_2O$  and  $NH_3\text{--}H_2S$  systems. *Icarus* 10, 365.
- Little, B., Anger, Clifford D., Ingersoll, A.P., Vasavada, A.R., Senske, D.A., Breneman, H.H., Borucki, W.J., the Galileo SSI Team, 1999. Galileo images of lightning on Jupiter. *Icarus* 142, 306–323.
- Mahaffy, P.R., Niemann, H.B., Demick, J., 1999. Measurement of ammonia at Jupiter with the Galileo probe mass spectrometer. *Bull. Am. Astron. Soc.* 31, 1154.
- Mizuno, H., Nakazawa, K., Hayashi, C., 1978. Instability of a gaseous envelope surrounding a planetary core and formation of giant planets. *Prog. Theoret. Phys.* 60 (3), 699–710.
- Nakajima, K., Takehiro, S., Ishiwatari, M., Hayashi, Y.-Y., 2000. Numerical modeling of Jupiter's moist convection layer. *Geophys. Res. Lett.* 27 (19), 3129–3132.
- Niemann, H.B., Harpold, D.N., Atreya, S.K., Carignan, Hunten, D.M., Owen, T.C., 1992. Galileo probe mass spectrometer experiment. *Space Sci. Rev.* 60, 111–142.
- Niemann, H.B., Atreya, S.K., Carignan, G.R., Donahue, T.M., Haberman, J.A., Harpold, D.N., Hartle, R.E., Hunten, D.M., Kasprzak, W.T., Mahaffy, P.R., Owen, T.C., Spencer, N.W., Way, S.H., 1996. The Galileo probe mass spectrometer: composition of Jupiter's atmosphere. *Science* 272, 846–849.
- Niemann, H.B., Atreya, S.K., Carignan, G.R., Donahue, T.M., Haberman, J.A., Harpold, D.N., Hartle, R.E., Hunten, D.M., Kasprzak, W.T., Mahaffy, P.R., Owen, T.C., Way, S.H., 1998. The composition of the jovian atmosphere as determined by the Galileo probe mass spectrometer. *J. Geophys. Res.* 103, 22831–22846.
- Nixon, C.A., Irwin, P.G.J., Calcutt, S.B., Taylor, F.W., Carlson, R.W., 2001. Atmospheric composition and cloud structure in jovian 5- $\mu\text{m}$  hotspots from analysis of Galileo NIMS measurements. *Icarus* 150, 48–68.
- Owen, T.C., Atreya, S.K., Mahaffy, P., Niemann, H.B., Wong, M.H., 1997. On the origin of Jupiter's atmosphere and the volatiles on the Medicean Stars. In: Barbieri, C., Rahe, J.H., Johnson, T.V., Sohus, A.M. (Eds.), *Three Galileos: The Man, The Spacecraft, The Telescope*. Kluwer Academic, Dordrecht, The Netherlands, pp. 289–297.
- Owen, T., Mahaffy, P., Niemann, H.B., Atreya, S., Donahue, T., Bar-Nun, A., de Pater, I., 1999. A low-temperature origin for the planetesimals that formed Jupiter. *Nature* 402 (6759), 269–270.
- Owen, T.C., Niemann, H.B., Mahaffy, P.R., 2001a. Nitrogen on the Moon: what does it tell us? *Earth Moon Planets* 85–86, 343–350.
- Owen, T.C., Niemann, H.B., Mahaffy, P.R., Atreya, S.K., Wong, M.H., 2001b. Protosolar nitrogen. *Astrophys. J.* 553, L77–L79.
- Perri, F., Cameron, A.G.W., 1974. Hydrodynamic instability of the solar nebula in the presence of a planetary core. *Icarus* 22, 416–425.
- Platten, J.K., Legros, J.C., 1984. *Convection in Liquids*. Springer-Verlag, New York, NY.
- Podolak, M., Hubbard, W.B., Pollack, J.B., 1993. Gaseous accretion and the formation of giant planets. In: Levy, E.H., Lunine, J.I. (Eds.), *Protostars and Planets III*. Univ. of Arizona Press, Tucson, AZ, pp. 1109–1147.
- Romani, P.N., de Pater, I., Dunn, D., Zahnle, K., Washington, B., 2000. Adsorption of ammonia onto ammonium hydrosulfide cloud particles in Jupiter's atmosphere. *Bull. Am. Astron. Soc.* 32, 997.
- Roos-Serote, M., Drossart, P., Encrenaz, Th., Carlson, R.W., Leader, F., 1999. Constraints on the tropospheric cloud structure of Jupiter from spectroscopy in the 5- $\mu\text{m}$  region: a comparison between Voyager/IRIS, Galileo-NIMS, and ISO-SWS spectra. *Icarus* 137, 315–340.
- Roos-Serote, M., Atreya, S.K., Wong, M.H., Drossart, P., 2004. On the water abundance in the atmosphere of Jupiter. *Planet. Space Sci.* 52, 397–414.
- Sault, R.J., Engel, C., de Pater, I., 2004. Longitude-resolved imaging of Jupiter at  $\lambda = 2\text{ cm}$ . *Icarus* 168, 336–343.
- Seiff, A., Kirk, D.B., Knight, T.C.D., Young, R.E., Mihalov, J.D., Young, L.A., Milos, F.S., Schubert, G., Blanchard, R.C., Atkinson, D., 1998. Thermal structure of Jupiter's atmosphere near the edge of a 5- $\mu\text{m}$  hot spot in the north equatorial belt. *J. Geophys. Res.* 103, 22857–22889.
- Showman, A.P., Dowling, T.E., 2000. Nonlinear simulations of Jupiter's 5-micron hot spots. *Science* 289, 1737–1740.

- Showman, A.P., Ingersoll, A.P., 1998. Interpretation of Galileo probe data and implications for Jupiter's dry downdrafts. *Icarus* 132, 205–220.
- Sigurdsson, S., Richer, H.B., Hansen, B.M., Stairs, I.H., Thorsett, S.E., 2003. A young white dwarf companion to pulsar B1620-26: evidence for early planet formation. *Science* 301, 193–196.
- Simon-Miller, A.A., Conrath, B., Gierasch, P.J., Beebe, R.F., 2000. A detection of water ice on Jupiter with Voyager IRIS. *Icarus* 145, 454–461.
- Smith, B.A., Soderblom, L.A., Johnson, T.V., Ingersoll, A.P., Collins, S.A., Shoemaker, E.M., Hunt, G.E., Masursky, H., Carr, M.H., Davies, M.E., Cook, A.F., Boyce, J.M., Owen, T., Danielson, G.E., Sagan, C., Beebe, R.F., Ververka, J., McCauley, J.F., Strom, R.G., Morrison, D., Briggs, G.A., Suomi, V.E., 1979. The Jupiter system through the eyes of Voyager 1. *Science* 204, 951–972.
- Sromovsky, L.A., Collard, A.D., Fry, P.M., Orton, G.S., Lemmon, M.T., Tomasko, M.G., Freedman, R.S., 1998. Galileo probe measurements of thermal and solar radiation fluxes in the jovian atmosphere. *J. Geophys. Res.* 103, 22929–22978.
- Stevenson, D.J., 1979. Semiconvection as the occasional breaking of weakly amplified internal waves. *Mon. Not. R. Astron. Soc.* 187, 129–144.
- Turner, J.S., 1968. The behavior of a stable salinity gradient heated from below. *J. Fluid Mech.* 33 (1), 183–200.
- Weidenschilling, S.J., Lewis, J.S., 1973. Atmospheric and cloud structure of the jovian planets. *Icarus* 20, 465–476.
- Wong, M.H., 2001. Hydrocarbons and condensible volatiles of Jupiter's Galileo probe entry site. PhD thesis. The University of Michigan, Ann Arbor, MI.
- Wong, M.H., Mahaffy, P.R., 2001. Revised deep water mixing ratio in the Galileo probe entry site from GPMS measurements. *Bull. Am. Astron. Soc.* 33, 1043.
- Wong, M.H., Atreya, S.K., Romani, P.N., 1998. Downdraft entrainment model. *Bull. Am. Astron. Soc.* 30, 1075.
- Wong, M.H., Atreya, S.K., Mahaffy, P.R., 1999. Error analysis of Galileo probe mass spectrometer atmospheric mixing ratio measurements. *Bull. Am. Astron. Soc.* 31, 1154.